

# EROAM: Event-based Camera Rotational Odometry and Mapping in Real-time

Wanli Xing<sup>1,2</sup>, Shijie Lin<sup>1,2</sup>, Linhan Yang<sup>1,2</sup>, Zeqing Zhang<sup>1,2</sup>, Yanjun Du<sup>3</sup>,  
Maolin Lei<sup>4</sup>, Yipeng Pan<sup>1,2</sup>, and Jia Pan<sup>1,2†</sup>

**Abstract**—This paper presents EROAM, a novel event-based rotational odometry and mapping system that achieves real-time, accurate camera rotation estimation. Unlike existing approaches that rely on event generation models or contrast maximization, EROAM employs a spherical event representation by projecting events onto a unit sphere and introduces Event Spherical Iterative Closest Point (ES-ICP), a novel geometric optimization framework designed specifically for event camera data. The spherical representation simplifies rotational motion formulation while enabling continuous mapping for enhanced spatial resolution. Combined with parallel point-to-line optimization, EROAM achieves efficient computation without compromising accuracy. Extensive experiments on both synthetic and real-world datasets show that EROAM significantly outperforms state-of-the-art methods in terms of accuracy, robustness, and computational efficiency. Our method maintains consistent performance under challenging conditions, including high angular velocities and extended sequences, where other methods often fail or show significant drift. Additionally, EROAM produces high-quality panoramic reconstructions with preserved fine structural details.

**Index Terms**—Event-based Vision, Simultaneous localization and mapping (SLAM).

VIDEO, SOURCE CODE AND DATA

Project page: <https://wlxing1901.github.io/eroam/>

## I. INTRODUCTION

**R**OTATIONAL motion estimation represents a fundamental challenge in computer vision and robotics, serving as a cornerstone for various applications from visual odometry to camera stabilization and panoramic image creation [1]. While traditional frame-based cameras have been widely used for this task, they struggle with rapid rotations due to inherent limitations such as motion blur, limited exposure control, and large inter-frame displacements that compromise data association and motion estimation accuracy.

Event cameras [2]–[4] offer a promising alternative through their bio-inspired design. Unlike conventional cameras that capture intensity frames at fixed intervals, these sensors operate asynchronously, measuring and reporting per-pixel brightness changes with microsecond precision. Each event is en-

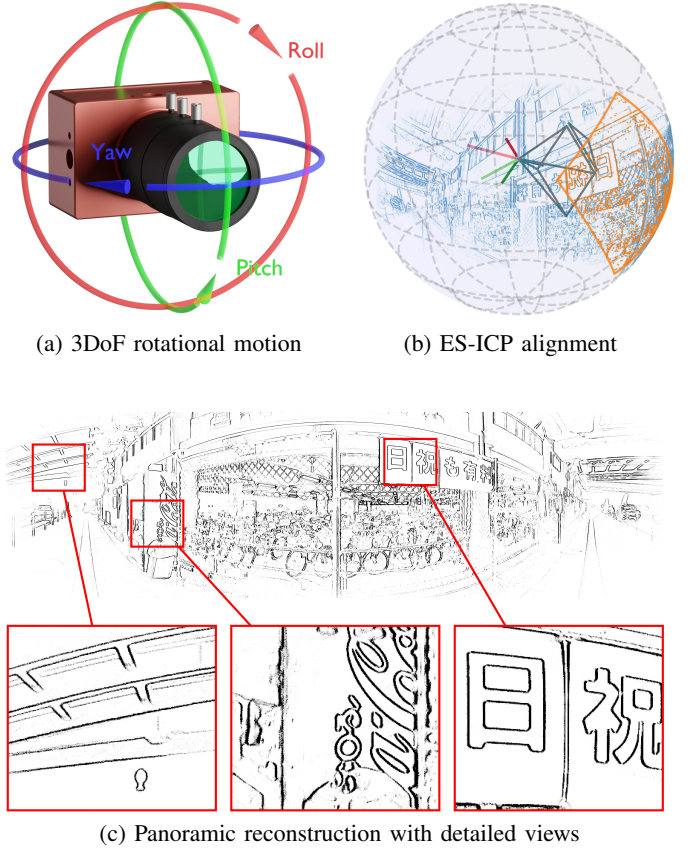


Fig. 1: Event-based 3DoF camera pose estimation and panoramic reconstruction. (a) Our method accurately estimates the 3DoF pose of an event camera from continuous event streams. (b) Events are projected onto a unit sphere and aligned using our novel Event Spherical Iterative Closest Point (ES-ICP) algorithm. (c) The aligned event sphere enables the reconstruction of a clear panoramic image with preserved fine details.

coded as a tuple  $e_k = (\mathbf{x}_k, t_k, p_k)$ , where  $\mathbf{x}_k = (u_k, v_k)^T$  denotes the pixel location,  $t_k$  the timestamp, and  $p_k$  the polarity of the brightness change [5]. This unique operating principle enables exceptional temporal resolution, high dynamic range (up to 140 dB), and low power consumption (20 mW) [4], making event cameras particularly well-suited for challenging scenarios involving high-speed motion or extreme lighting conditions.

The advantages of event cameras have been demonstrated across numerous applications, including SLAM [6]–[11], robotic navigation [12]–[15], feature extraction [16]–[19],

<sup>1</sup>Department of Computer Science, The University of Hong Kong, Hong Kong SAR, China. e-mail: wlxing@connect.hku.hk

<sup>2</sup>Centre for Transformative Garment Production, Hong Kong SAR, China.

<sup>3</sup>Department of Mechanical and Automation Engineering, The Chinese University of Hong Kong, Hong Kong SAR, China.

<sup>4</sup>Humanoids and Human Centered Mechatronics Research Line, Istituto Italiano Di Tecnologia (IIT), Genoa, Italy.

<sup>†</sup>Corresponding author.

optical flow estimation [20]–[23], video enhancement [24]–[26], 3D reconstruction [27]–[30], and optical systems [31]–[34]. Recent manufacturing advances have further accelerated their adoption by enabling higher-resolution sensors at more accessible price points [35].

In the specific context of rotational motion estimation, event cameras offer unique advantages through their high temporal resolution and freedom from motion blur, enabling potential accurate capture of rapid rotational movements that conventional cameras struggle to handle. Existing event-based approaches broadly fall into two categories. Event Generation Model (EGM) based methods [36], [37] explicitly model the event triggering process, requiring careful consideration of the contrast threshold and event generation mechanisms. In contrast, Contrast Maximization (CM) based approaches [5], [38], [39] estimate angular velocity by optimizing the alignment of events over temporal windows. While both approaches have demonstrated promising performance in scenarios with moderate and short-term rotational motion, they face significant challenges in more complex scenarios: EGM methods struggle with the complexity of accurately modeling event generation, while CM techniques may lack robustness during highly dynamic rotations involving rapid direction changes. Moreover, both approaches operate on discretized representations with predefined resolutions, introducing inherent quantization errors. Beyond these algorithmic limitations, both approaches often incur substantial computational overhead, limiting their real-time applicability.

Drawing inspiration from successful techniques in LiDAR SLAM [40]–[44], we propose a novel approach that addresses these limitations. As illustrated in Fig. 1, our method introduces two key innovations: a spherical event representation and the Event Spherical Iterative Closest Point (ES-ICP) algorithm. The spherical representation projects events onto a unit sphere, assigning continuous  $\mathbb{R}^3$  coordinates instead of working with discrete pixel locations. ES-ICP is a novel geometric optimization framework specifically designed for event data, which efficiently aligns sparse event point clouds on the unit sphere through parallel point-to-line optimization. Unlike existing methods that operate on discretized maps with fixed resolutions, our approach maintains both tracking and mapping in continuous spherical space, completely decoupling the core estimation pipeline from any discretization requirements. This continuous representation, combined with the innovative ES-ICP algorithm, not only enables precise motion estimation but also allows for flexible panoramic image generation at arbitrary resolutions as a post-processing step. The result is a real-time capable system that provides accurate and robust event camera rotation estimation.

Our main contributions are:

- 1) We introduce a novel spherical event representation that operates entirely in continuous  $\mathbb{R}^3$  space, enabling accurate motion estimation while decoupling the tracking process from panorama generation, which allows for flexible panoramic image creation at arbitrary resolutions;
- 2) We develop the Event Spherical Iterative Closest Point (ES-ICP) algorithm, which efficiently matches and

aligns event projections in continuous spherical space for robust rotational motion estimation;

- 3) We conduct comprehensive experimental validation on both synthetic and real-world datasets, demonstrating superior accuracy and robustness across diverse scenarios, and release our complete implementation and datasets to benefit the research community.

## II. RELATED WORKS

Event-based rotational motion estimation presents unique challenges and opportunities due to the asynchronous nature of event cameras. As summarized in Tab. I, existing approaches have evolved along two main paradigms: Event Generation Model (EGM) based methods, which explicitly model the event triggering process, and Contrast Maximization (CM) based methods, which focus on event alignment optimization. This section analyzes the fundamental principles, practical implementations, and inherent limitations of each approach, providing insights into their relative strengths and weaknesses.

### A. Event Generation Model Based Methods

The foundation of EGM-based approaches lies in modeling the precise conditions under which events are triggered. These methods explicitly consider the relationship between intensity changes and event generation, providing a theoretical framework for motion estimation. The basic principle states that an event is triggered when the change in log intensity exceeds a threshold  $C$ :

$$\Delta L(\mathbf{x}_k, t_k) = L(\mathbf{x}_k, t_k) - L(\mathbf{x}_k, t_k - \Delta t_k) = p_k C \quad (1)$$

where  $\mathbf{x}_k = (u_k, v_k)^\top$  represents the pixel coordinates,  $L(\mathbf{x}_k, t_k)$  is the log intensity at pixel  $\mathbf{x}_k$  at time  $t_k$ ,  $\Delta t_k$  is the time elapsed since the last event at the same pixel,  $p_k \in \{+1, -1\}$  is the polarity of the event, and  $C > 0$  is the contrast threshold [2], [4].

In practice, real event cameras exhibit more complex behavior due to sensor noise, transistor mismatch, and varying illumination conditions. This probabilistic nature is often modeled using normal distributions centered at the contrast threshold  $C$  [2], [45], [46]. For small time intervals  $\Delta t_k$ , the relationship between events and temporal brightness changes can be approximated as:

$$\frac{\partial L}{\partial t}(\mathbf{x}_k, t_k) \approx \frac{p_k C}{\Delta t_k} \quad (2)$$

This approximation serves as the foundation for various event-based algorithms [47]–[50].

1) *Simultaneous Mosaicing and Tracking (SMT)*: SMT [36] introduced the first comprehensive approach to event-based visual processing by simultaneously addressing camera tracking and scene reconstruction. The method employs a dual-filter architecture: a particle filter for camera rotation tracking and pixel-wise Extended Kalman Filters (EKFs) for mapping. In the tracking module, camera poses are estimated by evaluating how well each pose hypothesis aligns with the current gradient map using an event likelihood model. Concurrently, the mapping module maintains and updates a

TABLE I: Comparison of Event-based Rotational Motion Estimation Methods

Method	Principle	Real-time	GPU Required	Map Storage	Threshold $C$ Dependency	Polarity Dependency
SMT [36]	EGM	No	No	Discrete	Yes	Yes
RTPT [37]	EGM	No	Yes	Discrete	No	No
CM-GAE [39]	Contrast Maximization	No	No	Discrete	No	Yes
CMax-SLAM [38]	Contrast Maximization	No	No	Discrete	No	No
EROAM (ours)	ES-ICP	Yes	No	Continuous	No	No

gradient map through EKF filtering of incoming events, with each pixel independently tracking its gradient estimate and uncertainty.

The key innovation of SMT lies in its probabilistic treatment of both tracking and mapping components, which work symbiotically: the tracker leverages the gradient map for pose evaluation, while the mapping system utilizes pose estimates for gradient updates. This approach effectively handles the asynchronous nature of event data while maintaining a coherent scene representation.

2) *Real-Time Panoramic Tracking (RTPT)*: RTPT [37] advances event-based motion estimation through a direct optimization approach. The method introduces a probabilistic map that tracks event occurrence likelihoods at each spatial location, dynamically updating as the camera moves. Camera pose estimation is formulated as an energy minimization problem that elegantly combines re-projection error with temporal motion smoothness.

A significant contribution of RTPT is its probabilistic map representation, which maintains both observed event counts and possible event occurrences for each location. This formulation naturally accommodates the sparse and asynchronous characteristics of event data while preserving scene geometry in map updates. However, achieving real-time performance requires GPU acceleration, and the method faces challenges with map updates at higher resolutions.

**Limitations of EGM Based Methods.** EGM-based approaches face several fundamental challenges:

- Both SMT and RTPT struggle with robustness to sensor noise and varying illumination conditions, despite their different approaches to handling contrast threshold specification.
- The computational requirements for map updates become prohibitive at higher resolutions, even with GPU acceleration.
- The use of discretized map storage inherently introduces quantization errors that affect motion estimation accuracy.

### B. Contrast Maximization Based Methods

The contrast maximization framework, introduced by Gallego and Scaramuzza [5], [51], represents a fundamentally different approach to event-based motion estimation. The key insight is that when events are warped (rotated) according to the true motion parameters, they align to create sharp edge patterns.

The framework formulates motion estimation as an optimization problem:

$$\omega^* = \operatorname{argmax}_{\omega} \operatorname{Var}(I(\omega, \mathcal{E})) \quad (3)$$

where  $\omega$  is the angular velocity vector to be estimated, and  $I(\omega, \mathcal{E})$  represents an image formed by warped events. This image is created by:

$$I(\mathbf{x}; \omega) = \sum_k \pm_k \delta(\mathbf{x} - \mathbf{x}'_k(\omega)) \quad (4)$$

where  $\pm_k$  is the polarity of each event, and  $\mathbf{x}'_k(\omega)$  represents the warped (rotated) position of the original event according to the candidate angular velocity  $\omega$ . The Dirac delta function  $\delta$  accumulates event polarities at the warped locations.

The quality of motion estimation is measured through the image variance:

$$\operatorname{Var}(I(\omega, \mathcal{E})) = \frac{1}{|\Omega|} \int_{\Omega} (I(\omega, \mathcal{E})(\mathbf{x}) - \mu(I(\omega, \mathcal{E})))^2 d\mathbf{x} \quad (5)$$

where  $\Omega$  is the image domain. The variance measures the contrast of the warped event image - when events are correctly aligned according to the true motion, they form sharp edges resulting in maximum contrast.

1) *Global Events Alignment for Rotational Motion Estimation (CM-GAE)*: CM-GAE [39] enhances the contrast maximization framework through a dual-optimization strategy aimed at reducing drift. The method maintains a global event image by continuously aligning observed events to the initial camera coordinate frame, enabling both local and global consistency checks. Beyond maximizing contrast within temporal windows, CM-GAE introduces a second optimization step that aligns locally warped event images with the accumulated global event image, effectively reducing the drift accumulation common in local optimization methods.

2) *Event-based Rotational SLAM System (CMax-SLAM)*: CMax-SLAM [38] represents a significant advancement as the first complete event-based rotational SLAM system incorporating both front-end and back-end components. The front-end employs contrast maximization for angular velocity estimation, while the back-end performs continuous-time trajectory refinement using B-splines. A key innovation lies in its formulation of bundle adjustment based on contrast maximization, optimizing camera trajectories while simultaneously generating sharp panoramic maps as a by-product of the optimization process.

**Limitations of CM Based Methods.** Contrast maximization approaches face several key challenges:

- The temporal window selection presents an inherent trade-off between having sufficient events for optimization and maintaining the constant angular velocity assumption.
- Iterative optimization and repeated event warping operations impose significant computational overhead.

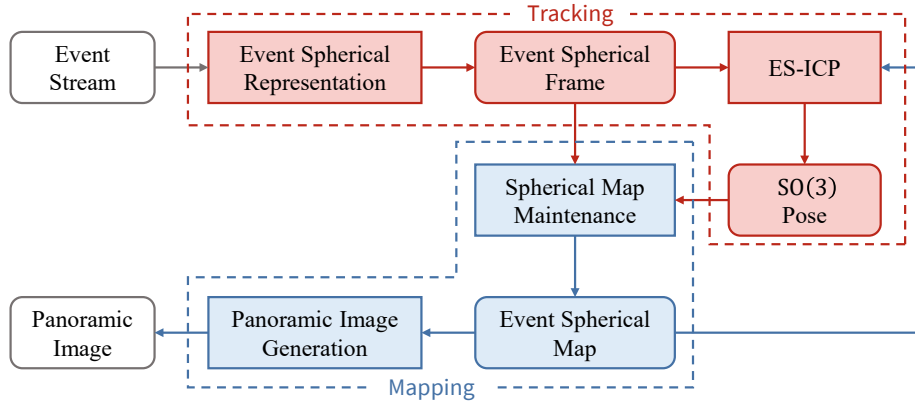


Fig. 2: System Overview: The proposed event-based rotational motion estimation system consists of two main modules. The **tracking module** processes event streams to estimate  $SO(3)$  pose using spherical representation and ES-ICP. The **mapping module** maintains and updates the spherical event map, which supports both tracking and panoramic image generation.

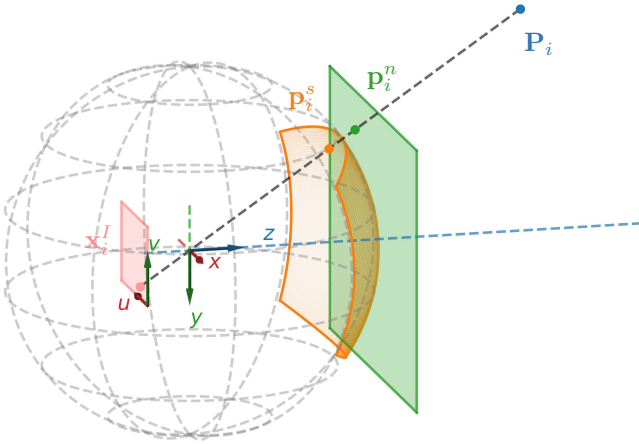


Fig. 3: Spherical projection process: The 3D point  $P_i$  is first projected onto the image plane as  $x_i^I$ . After undistortion and normalization, it becomes  $p_i^n$  on the normalized image plane. Finally,  $p_i^n$  is projected onto the unit sphere, resulting in the spherical point  $p_i^s$ .

- The optimization process can encounter local optima [52] and degenerate solutions affecting estimation reliability.
- Global optimization approaches introduce substantial computational demands that impact real-time performance.

### III. METHODOLOGY

#### A. System Overview

Our proposed event-based rotational motion estimation system, illustrated in Fig. 2, comprises two main components: a tracking module and a mapping module. The system processes incoming event streams through a series of steps to estimate the camera’s  $SO(3)$  pose and construct a spherical event map.

The tracking module begins by transforming incoming events into a spherical representation (III-B). These spherical events are then grouped into event frames and undergo motion compensation (III-C). The compensated event frames serve as

input for our novel Event Spherical Iterative Closest Point (ES-ICP) algorithm (III-D). The ES-ICP algorithm estimates the camera’s rotational pose in  $SO(3)$ , leveraging the spherical event map maintained by the mapping module.

Concurrently, the mapping module selectively updates the spherical event map using key frames determined by significant rotational motion (III-E). This updated map not only aids in subsequent tracking iterations but also serves as the basis for panoramic image generation (III-F).

This iterative process of tracking and mapping enables robust and high-frequency rotation estimation in  $SO(3)$  space, while simultaneously constructing and maintaining a comprehensive spherical event map from the incoming event data.

Tab. II summarizes the key symbols and variables used throughout our methodology.

#### B. Event Spherical Representation

In event-based rotational motion estimation, the choice of event representation is crucial for both accuracy and computational efficiency. We propose a spherical representation of events, which offers two significant advantages over traditional pixel-plane approaches: 1) Simplification of rotational motion formula, and 2) Enhanced spatial resolution and continuous mapping.

1) *Simplified Motion Geometry on Unit Sphere:* In pure rotational motion, considering events on the pixel plane involves a complex series of transformations including rotation, perspective projection, and distortion. Fig. 3 illustrates this process, showing the transformation from a 3D point to its spherical representation. Let’s consider a 3D point  $P_i$  and its projection onto the image plane  $x_i^I$ . The process can be described as follows [53]:

$$\mathbf{x}_i^I = \mathbf{f}(\mathbf{K}[\mathbf{R}|\mathbf{t}]\mathbf{P}_i) \quad (6)$$

where  $\mathbf{K}$  is the camera intrinsic matrix,  $\mathbf{f}$  is the distortion function, and  $[\mathbf{R}|\mathbf{t}]$  represents the rigid body transformation from the world coordinate system to the camera coordinate system.

TABLE II: Summary of Key Symbols and Variables

Symbol	Description
$e_i$	Individual event $(u_i, v_i, t_i, p_i)$
$\mathbf{x}_i^I$	Pixel coordinates $(u_i, v_i)^T$
$\mathbf{K}$	Camera intrinsic matrix
$\mathbf{f}(\cdot)$	Distortion function
$\mathbf{f}^{-1}(\cdot)$	Undistortion function
$\mathbf{x}_i^u$	Undistorted pixel coordinates
$\mathbf{p}_i^n$	Normalized coordinates on virtual imaging plane
$\mathbf{p}_i^s$	Spherical representation of an event
$\mathbf{p}_i^c$	Cylindrical projection of a point
$\mathcal{E}^s$	Event spherical frame
$f$	Event spherical frame formation frequency
$n$	Number of events per spherical frame
$\mathbf{R}$	Rotation matrix in $SO(3)$
$\mathbf{t}$	Translation vector
$\omega$	Angular velocity of the event camera
$\mathcal{M}^s$	Spherical event map
$\theta_t$	Rotation threshold for key frames
$\mathbf{d}$	Direction vector of fitted line (ES-ICP)
$\mathbf{c}$	Point on fitted line (ES-ICP)
$\mathbf{J}_i$	Jacobian matrix for each point (ES-ICP)
$\mathbf{H}$	Approximated Hessian matrix (ES-ICP)
$\Delta \mathbf{x}$	Incremental update in $\mathfrak{so}(3)$ (ES-ICP)
$\mathbf{g}$	Gradient vector (ES-ICP)
$\mathbf{q}_b^s$	Centroid of points in a voxel bin (map update)
$N_b$	Number of points in a voxel bin
$\phi_v$	Vertical field of view (panoramic)
$\phi_h$	Horizontal span angle (panoramic)
$\exp(\cdot^\wedge)$	Exponential map from $\mathfrak{so}(3)$ to $SO(3)$
$\log(\cdot^\vee)$	Logarithm map from $SO(3)$ to $\mathfrak{so}(3)$
$(\cdot)^\wedge$	Hat operator (vector to skew-symmetric matrix)
$(\cdot)^\vee$	Vee operator (skew-symmetric matrix to vector)
$\ \cdot\ _2$	Euclidean (L2) norm

Now, consider the same point  $\mathbf{P}_i$  observed from two camera views  $I_1$  and  $I_2$  related by a rotation  $\mathbf{R}_{12}$  (denoting the rotation from reference frame 2 to reference frame 1, and  $\mathbf{t}_{12} = \mathbf{0}$ ). The corresponding pixel coordinates in the two views,  $\mathbf{x}_i^{I_1}$  and  $\mathbf{x}_i^{I_2}$ , are related by:

$$\mathbf{x}_i^{I_1} = \mathbf{f}(\mathbf{K}\mathbf{R}_{12}\mathbf{K}^{-1}\mathbf{f}^{-1}(\mathbf{x}_i^{I_2})) \quad (7)$$

where  $\mathbf{f}^{-1}$  is the undistortion function. This expression, involving multiple non-linear transformations, is both mathematically complex and computationally demanding.

In contrast, on a unit sphere, the projection of a 3D point  $\mathbf{P}_i$  can be expressed as:

$$\mathbf{p}_i^s = \frac{[\mathbf{R}|\mathbf{t}]\mathbf{P}_i}{\|[\mathbf{R}|\mathbf{t}]\mathbf{P}_i\|_2} \quad (8)$$

For pure rotational motion,  $\mathbf{t} = \mathbf{0}$ . Moreover, since  $\mathbf{R}$  is a rotation matrix, its determinant is 1, which preserves the vector's magnitude. Therefore, the equation simplifies to:

$$\mathbf{p}_i^s = \frac{\mathbf{R}\mathbf{P}_i}{\|\mathbf{P}_i\|_2} \quad (9)$$

Consequently, for two spherical projections  $\mathbf{p}_i^{s1}$  and  $\mathbf{p}_i^{s2}$  from views differing by a rotation  $\mathbf{R}_{12}$ , we have:

$$\mathbf{p}_i^{s1} = \mathbf{R}_{12}\mathbf{p}_i^{s2} \quad (10)$$

This formulation provides a direct and simple representation of rotational motion on the unit sphere, significantly reducing computational complexity compared to the pixel-plane formulation.

2) *Enhanced Spatial Resolution and Continuous Mapping:* While event cameras provide discrete pixel locations, our spherical representation offers significant advantages in spatial resolution and mapping continuity. On the pixel plane, each event is confined to a discrete grid, with each pixel corresponding to a specific field of view (FOV). This discretization limits the precision of motion estimation, as movements within a single pixel's FOV become indistinguishable.

In contrast, the spherical representation, although derived from discrete pixel data, allows for a more nuanced positioning of events in 3D space. This approach enables us to maintain sub-pixel precision in event positioning, as the spherical coordinates are not confined to a discrete grid. Consequently, we can create a continuous map of the environment, where events can be placed at arbitrary positions on the unit sphere. This enhanced spatial resolution is particularly beneficial for representing and tracking small motions, even when they don't result in a change of pixel coordinates.

Fig. 4 illustrates this advantage, showing how a small camera rotation can lead to a detectable change in the spherical representation ( $\Delta \mathbf{p}_i^s$ ), while potentially resulting in no change in the pixel coordinates ( $\Delta \mathbf{x}_i^I = 0$ ). This capability significantly enhances the precision of our rotation estimation algorithm, allowing for more accurate tracking of camera motion.

Given these advantages, we implement the Event Spherical Representation as follows:

Given an event  $e_i = (\mathbf{x}_i^I, t_i, p_i)$ , where  $\mathbf{x}_i^I = (u_i, v_i)^T$  denotes the pixel coordinates,  $t_i$  the timestamp, and  $p_i$  the polarity, we perform the following steps (illustrated in Fig. 3):

1) **Undistortion:** First, we undistort the pixel coordinates  $\mathbf{x}_i^I$  using the camera's intrinsic parameters and distortion coefficients:

$$\mathbf{x}_i^u = \mathbf{f}^{-1}(\mathbf{x}_i^I) \quad (11)$$

2) **Normalization:** We then normalize the undistorted coordinates using the camera's intrinsic matrix  $\mathbf{K}$ :

$$\mathbf{p}_i^n = \mathbf{K}^{-1} \begin{pmatrix} \mathbf{x}_i^u \\ 1 \end{pmatrix} \quad (12)$$

3) **Spherical Projection:** Finally, we project the normalized coordinates onto the unit sphere:

$$\mathbf{p}_i^s = \frac{\mathbf{p}_i^n}{\|\mathbf{p}_i^n\|_2} \quad (13)$$

The resulting  $\mathbf{p}_i^s$  is a 3D point on the unit sphere, representing the direction of the event in 3D space. This spherical representation allows us to treat events as points on a continuous surface, facilitating more accurate rotational motion estimation.

### C. Event Spherical Frame Formation

The continuous nature of event streams reflects the ongoing motion of the event camera. While contrast maximization methods typically process events over relatively long time windows (e.g., 0.1 s) under the assumption of constant angular velocity, we propose a different approach that operates on

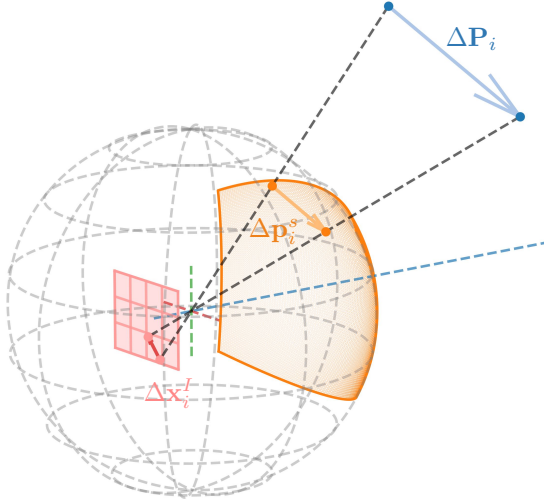


Fig. 4: Illustration of motion sensitivity differences between spherical and pixel representations. When the event camera undergoes a small rotation, the 3D point position relative to the camera changes by  $\Delta P_i$ . This results in a measurable change  $\Delta p_i^s$  on the spherical surface. However, in the pixel coordinate system, the motion may not cause a change in pixel location, resulting in  $\Delta x_i^f = 0$ . This demonstrates the higher sensitivity and continuous nature of the spherical representation compared to the discrete pixel representation.

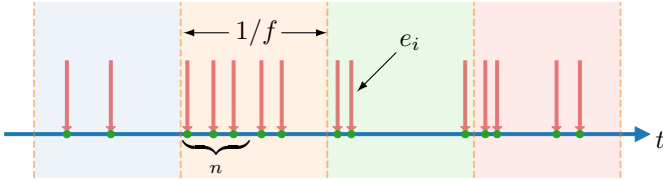


Fig. 5: Event spherical frame formation process: Each downward arrow represents a triggered event  $e_i$ . Colored backgrounds indicate time segments of duration  $1/f$ . The brace underneath shows the selection of the first  $n$  events within each time segment to form an event spherical frame.

much shorter time scales to better handle varying motion patterns. We segment the event stream at a frequency  $f$  and select the first  $n$  events from each segment, as illustrated in Fig. 5. These events are then transformed into spherical coordinates as described in Section III-B to form event spherical frames.

To illustrate why our frame selection strategy effectively minimizes intra-frame camera motion, let us analyze a specific example from our implementation on ECRot [38] dataset. For ECRot sequences, we set  $f = 1000$  Hz and  $n = 1500$ . Our analysis shows that these  $n = 1500$  events span an average duration of only 0.121 ms. Taking the average angular velocity of  $\omega = 120^\circ/\text{s}$  as an example, this brief time span results in an intra-frame rotation of  $0.0145^\circ$ , leading to very small motion-induced pixel displacement within each frame. Each frame containing only 1500 events is too sparse to reveal the scene structure, making it challenging for contrast maximization methods to process effectively. However, our ES-ICP algorithm is specifically designed to handle such sparse point clouds effectively. This configuration allows our subsequent ES-ICP method to estimate  $SO(3)$  pose at 1000 Hz.

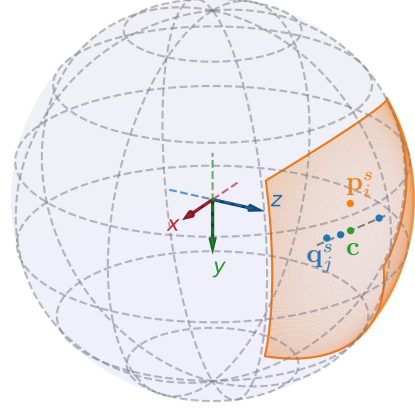


Fig. 6: ES-ICP error visualization. The shaded region represents the spherical event map  $\mathcal{M}^s$ . Our objective is to minimize the distances between all  $p_i^s$  in the current event frame and the line fitted to their  $k$  nearest neighbors  $q_j^s$  in the map. The point  $c$  represents the centroid of the  $k$  nearest neighbors used for line fitting.

Although the intra-frame motion is already very small, we further apply motion compensation to the events within each frame to achieve the highest possible accuracy. For each frame, we estimate a constant angular velocity  $\omega$  based on the rotational change between the two most recent pose estimates. Given this short time span (0.121 ms on average), the constant angular velocity assumption is much more reasonable compared to applying it over longer windows. Using this angular velocity, we then warp all events within the frame to the timestamp of the first event in the frame. Specifically, for an event  $e_i$  with timestamp  $t_i$  and its spherical representation  $p_i^s$ , we apply the following transformation:

$$p_i^s \leftarrow \exp((t_0 - t_i)\omega^\wedge) p_i^s \quad (14)$$

where  $t_0$  is the timestamp of the first event in the frame,  $t_i$  is the timestamp of the  $i$ -th event,  $\omega^\wedge$  denotes the skew-symmetric matrix of  $\omega$ , and  $\exp(\cdot^\wedge)$  is the exponential map from  $\mathfrak{so}(3)$  to  $SO(3)$ . After processing all  $n$  events, we obtain the motion-compensated event spherical frame  $\mathcal{E}^s = \{p_k^s\}_{k=0}^{n-1}$ .

#### D. Event Spherical Iterative Closest Point (ES-ICP) Algorithm

The core of our approach lies in the Event Spherical Iterative Closest Point (ES-ICP) algorithm, which is designed to efficiently estimate rotational motion using spherical event representations. As illustrated in Fig. 1b, our goal is to align the sparse event point cloud with a denser spherical event map on the surface of a unit sphere.

Since events are primarily triggered by edges in the environment, and these edges typically form continuous structures on the spherical surface, we optimize the distance between points and nearby line segments rather than point-to-point distances for improved robustness and accuracy. This approach better captures the underlying edge structure of the scene while being more resilient to noise and sparse event distributions. As visualized in Fig. 6, both the map and the frame exist on a

curved surface (the unit sphere), where these line segments locally approximate the edge structures projected onto the sphere.

Given a set of event projections on a unit sphere  $\mathcal{E}^s = \{\mathbf{p}_i^s\}_{i=0}^{n-1}$ , representing a sparse event spherical frame of  $n$  points, and a spherical event map  $\mathcal{M}^s = \{\mathbf{q}_j^s\}_{j=0}^{m-1}$ , which is an accumulated representation of previously aligned event frames, our objective is to optimize the pose  $\mathbf{R}$  in  $SO(3)$  to minimize the distance between points in  $\mathcal{E}^s$  and  $\mathcal{M}^s$ . This can be formulated as:

$$\mathbf{R}^* = \operatorname{argmin}_{\mathbf{R} \in SO(3)} \sum_{i=0}^{n-1} d(\mathbf{R}\mathbf{p}_i^s, \mathcal{M}^s) \quad (15)$$

where  $d(\cdot, \cdot)$  represents a distance metric and  $\mathbf{R}^*$  is the optimal rotation we seek to estimate.

To implement this approach, for each  $\mathbf{p}_i^s$ , we first apply the current estimate of the rotation matrix  $\mathbf{R} \in SO(3)$ :

$$\tilde{\mathbf{p}}_i^s = \mathbf{R}\mathbf{p}_i^s \quad (16)$$

We then employ a k-d tree structure to efficiently find the  $k$  nearest neighbors of  $\tilde{\mathbf{p}}_i^s$  in  $\mathcal{M}^s$ . Using these neighbors, we fit a line  $l: \mathbf{d}\tau + \mathbf{c}$ , where  $\mathbf{d}$  is the direction vector and  $\mathbf{c}$  is the centroid of the  $k$  nearest neighboring points. It's worth noting that while Fig. 6 illustrates this concept with exaggerated distances for clarity, in practice, the nearest neighbors are typically very close to each other on the unit sphere. As a result, the fitted line closely approximates the tangent to the unit sphere at that point.

The optimization problem can then be reformulated as:

$$\mathbf{R}^* = \operatorname{argmin}_{\mathbf{R} \in SO(3)} \sum_{i=0}^{n-1} \|\mathbf{d} \times (\mathbf{R}\mathbf{p}_i^s - \mathbf{c})\|_2^2 \quad (17)$$

We solve this non-linear least squares optimization problem using the Gauss-Newton method. For each point, we derive the Jacobian matrix  $\mathbf{J}_i \in \mathbb{R}^{3 \times 3}$  with respect to the Lie algebra of  $SO(3)$ :

$$\mathbf{J}_i = -\mathbf{d}^\wedge \mathbf{R}\mathbf{p}_i^{s\wedge} \quad (18)$$

where  $\mathbf{d}^\wedge$  and  $\mathbf{p}_i^{s\wedge}$  denote the skew-symmetric matrices of  $\mathbf{d}$  and  $\mathbf{p}_i^s$ , respectively.

In each Gauss-Newton iteration, we construct and solve the normal equation:

$$\mathbf{H}\Delta\mathbf{x} = \mathbf{g} \quad (19)$$

Here,  $\mathbf{H} \in \mathbb{R}^{3 \times 3}$  is the approximated Hessian matrix,  $\Delta\mathbf{x} \in \mathbb{R}^3$  is the incremental update we seek in the Lie algebra  $\mathfrak{so}(3)$ , and  $\mathbf{g} \in \mathbb{R}^3$  is the gradient vector. These are computed as:

$$\mathbf{H} = \sum_{i=0}^{n-1} \mathbf{J}_i^\top \mathbf{J}_i, \quad \mathbf{g} = -\sum_{i=0}^{n-1} \mathbf{J}_i^\top [\mathbf{d} \times (\mathbf{R}\mathbf{p}_i^s - \mathbf{c})] \quad (20)$$

After solving Eq. 19 to obtain the update  $\Delta\mathbf{x}$  in the Lie algebra  $\mathfrak{so}(3)$ , we update the current pose estimate  $\mathbf{R}_{it}$  using the exponential map:

$$\mathbf{R}_{it+1} = \mathbf{R}_{it} \exp(\Delta\mathbf{x}^\wedge) \quad (21)$$

where  $\exp(\cdot^\wedge)$  maps from  $\mathfrak{so}(3)$  to  $SO(3)$ , and  $it$  denotes the iteration number.

The optimization is considered converged when the magnitude of the update  $\|\Delta\mathbf{x}\|$  falls below a predefined threshold or reaches a maximum number of iterations, yielding an optimal rotation estimate that precisely aligns the event frame with the spherical map.

## E. Event Spherical Map Maintenance and Update

To maintain an accurate and efficient representation of the environment while managing computational resources, we selectively update our spherical event map based on significant camera motion. We designate certain frames as key frames based on a rotation threshold criterion, rather than incorporating every processed frame into the map.

Let  $\mathbf{R}_c$  be the current frame's estimated rotation and  $\mathbf{R}_k$  be the rotation of the last key frame. We consider the current frame as a new key frame if:

$$\|\log(\mathbf{R}_c \mathbf{R}_k^{-1})^\vee\|_2 > \theta_t \quad (22)$$

where  $\log(\cdot)^\vee$  is the logarithm map  $SO(3)$  to  $\mathfrak{so}(3)$ , and  $\theta_t$  is a predefined rotation threshold.

Upon identifying a new key frame, we initiate the map update process by merging the current map points  $\{\mathbf{q}_j^s\}_{j=0}^{m-1}$  with the newly aligned event frame points  $\{\mathbf{p}_i^s\}_{i=0}^{n-1}$  from the key frame. The merged point cloud is then processed using a voxel grid filter.

This voxel grid filter prevents the accumulation of redundant points in the same spatial region, which is critical for the point-to-line error metric used in ES-ICP. By ensuring a more uniform distribution of points, the filter helps maintain the integrity of our point-to-line approach, preventing the point-to-line error from degenerating into a point-to-point error in areas of high point density.

For each occupied voxel bin (denoted by subscript  $b$ ), we compute the centroid  $\mathbf{q}_b^s$  of all points within that bin:

$$\mathbf{q}_b^s = \frac{1}{N_b} \sum_{i=1}^{N_b} \mathbf{p}_i \quad (23)$$

where  $N_b$  represents the number of points in the voxel bin, and  $\mathbf{p}_i$  are the individual points within that voxel.

These centroids form a new, filtered point set  $\mathcal{M}_k^s = \{\mathbf{q}_b^s\}_{b=0}^{K-1}$ , where  $K$  is the total number of occupied voxel bins. To maintain the spherical nature of our map, we perform a normalization step for each centroid:

$$\mathbf{q}_b^s \leftarrow \frac{\mathbf{q}_b^s}{\|\mathbf{q}_b^s\|_2} \quad (24)$$

This normalization ensures that all points in our updated map  $\mathcal{M}_k^s$  reside on the unit sphere, preserving the geometric integrity of our spherical representation.

Our spherical voxel grid implementation ensures continuity and consistency across the entire unit sphere. This approach maintains uniform point distribution and preserves local geometric relationships, crucial for robust nearest neighbor searches and accurate line fitting in our ES-ICP algorithm across all spherical regions.

## F. Panoramic Image Generation

A valuable byproduct of our system is the generation of panoramic images. Due to the properties of our spherical event map, we can efficiently and conveniently obtain these panoramic representations. The conversion process involves projecting the events from the unit sphere onto a surrounding cylinder, which is then unwrapped to form a 2D panoramic

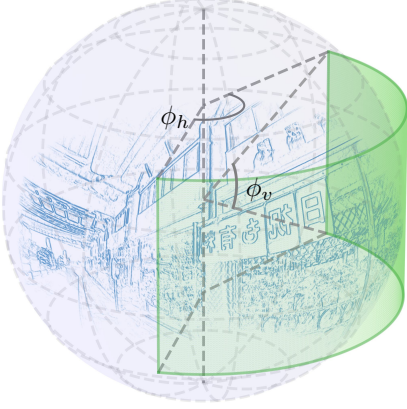


Fig. 7: Projection from spherical event map to panoramic image. Events on the unit sphere are projected onto a surrounding cylinder, then unwrapped to form the panorama.  $\phi_v$ : vertical field of view,  $\phi_h$ : horizontal span angle. The cylinder is discretized based on desired pixel density to generate the final panoramic image.

representation, as illustrated in Fig. 7. The projection process is defined by two key parameters:  $\phi_v$ , the vertical field of view, which determines the height of the cylindrical projection surface, and  $\phi_h$ , the horizontal span angle, which defines the width of the panoramic image. Fig. 1c shows an example of the resulting panoramic image generated by our method.

The conversion from spherical coordinates to panoramic image coordinates involves projecting each spherical point  $\mathbf{p}_i^s = (x, y, z)^T$  onto the cylinder surface using the equation:

$$\mathbf{p}_i^c = \left( \frac{x}{\sqrt{x^2 + y^2}}, \frac{y}{\sqrt{x^2 + y^2}}, \frac{z}{\sqrt{x^2 + y^2}} \right) \quad (25)$$

This projection normalizes the x and y coordinates to the unit circle while preserving the relative height of z. The cylinder surface is then discretized based on the desired pixel density of the panoramic image, with the azimuthal angle of the projected point determining its horizontal position and its height on the cylinder determining its vertical position in the image.

A key advantage of our approach is that the entire mapping process operates in continuous spherical space, maintaining complete independence from any discretization requirements. Unlike traditional methods that require predefined resolutions, our method allows for the generation of panoramic images at arbitrary resolutions as needed, with the panorama generation process entirely decoupled from the core tracking and mapping pipeline. This design choice offers several benefits:

- The spherical mapping and pose estimation operate in continuous space, ensuring their accuracy is independent of any discretization choices.
- Multiple panoramic images can be generated at different resolutions without modifying the underlying map data.
- The panorama generation serves as an independent post-processing step, preserving the real-time performance of the core system.

#### IV. EXPERIMENTS

In this section, we present a comprehensive evaluation of our proposed event-based rotational motion estimation method.

We begin by detailing our experimental setup, including evaluation metrics, datasets, and hardware configuration (IV-A). We then evaluate our method on both synthetic and real-world data: first on the ECRot dataset (IV-B), followed by extended simulations using ESIM (IV-C) to assess performance under various challenging conditions, and then on real-world sequences (IV-D). Finally, we provide a detailed runtime analysis across all experiments (IV-E).

##### A. Experimental Setup

1) *Evaluation Metrics*: To rigorously assess the performance of our proposed method, we employ two primary metrics for evaluating rotational motion estimation accuracy: Absolute Pose Error (APE) [54] and Relative Pose Error (RPE) [54]. These metrics provide a comprehensive evaluation of both global consistency and local accuracy of the estimated camera rotations.

a) *Absolute Pose Error (APE)*: The APE quantifies the global consistency of the estimated camera poses by measuring the discrepancy between the estimated rotation and the ground truth at each timestamp. For a given timestamp  $t_k$ , the absolute rotation error  $\epsilon_k$  is computed as:

$$\epsilon_k = \log(\mathbf{R}'_k{}^\top \mathbf{R}_k)^\vee \quad (26)$$

where  $\mathbf{R}_k$  is the estimated rotation at  $t_k$ ,  $\mathbf{R}'_k$  is the corresponding ground truth rotation, and  $\log(\cdot)^\vee$  is the composition of the logarithmic function and the vee operator, which together map an element of  $\text{SO}(3)$  to its corresponding element in  $\mathbb{R}^3$ . The magnitude of  $\epsilon_k$ , denoted as  $\|\epsilon_k\|_2$ , directly represents the angle (in radians) between the estimated and ground truth rotations.

To obtain a single representative value, we calculate the mean of these angular errors over all timestamps:

$$\overline{ape} = \frac{1}{N} \sum_{k=1}^N \|\epsilon_k\|_2 \quad (27)$$

where  $N$  is the total number of timestamps in the evaluated trajectory. This mean value  $\overline{ape}$  provides an average measure of the angular error across the entire trajectory.

b) *Relative Pose Error (RPE)*: The RPE measures the local accuracy of the pose estimates by comparing the relative rotation between two timestamps in the estimated trajectory to the corresponding relative rotation in the ground truth trajectory. For a pair of timestamps  $t_k$  and  $t_{k+\Delta}$ , the relative rotation error  $\delta_k$  is calculated as:

$$\delta_k = \log \left( (\mathbf{R}'_k{}^\top \mathbf{R}'_{k+\Delta})^{-1} (\mathbf{R}_k{}^\top \mathbf{R}_{k+\Delta}) \right)^\vee \quad (28)$$

where  $\{\mathbf{R}_k, \mathbf{R}_{k+\Delta}\}$  and  $\{\mathbf{R}'_k, \mathbf{R}'_{k+\Delta}\}$  are pairs of estimated and ground truth poses, respectively. Similar to the APE, the magnitude of  $\delta_k$ , denoted as  $\|\delta_k\|_2$ , represents the angular difference between the estimated and ground truth relative rotations.

The mean of these relative rotation errors  $\overline{rpe}$  is then computed as:

$$\overline{rpe} = \frac{1}{M} \sum_{k=1}^M \|\delta_k\|_2 \quad (29)$$

where  $M$  is the total number of relative pose pairs evaluated along the entire trajectory. To ensure fair comparison across



methods with different estimation frequencies, we compute the RPE at fixed intervals corresponding to  $10^\circ$  of rotation in the ground truth trajectory. Under this evaluation scheme, an  $\overline{rpe}$  value of  $0.5^\circ$  indicates that, on average, the estimated relative rotation between poses separated by  $10^\circ$  of ground truth motion differs from the true relative rotation by  $0.5^\circ$ . This approach provides a consistent measure of local accuracy across different methods, regardless of their specific output rates.

For the evaluation of APE and RPE across all experiments, we utilize the EVO toolkit [55], a software package designed for the evaluation of odometry and SLAM algorithms, ensuring consistent and reproducible assessments. To facilitate intuitive understanding of the error magnitudes, we convert all radian measurements to degrees in our reported results.

2) *Datasets*: To comprehensively evaluate our method’s accuracy and robustness in rotation estimation, we utilize three types of data sources: the ECRot synthetic dataset [38], extended simulations generated using the ESIM simulator [56], and our newly collected real-world sequences with LiDAR-based ground truth.

a) *ECRot Synthetic Dataset*: We utilize all six synthetic sequences from the ECRot dataset: bay, bicycle, city, street, town and playroom. The first five sequences feature a resolution of  $240 \times 180$  with a duration of 5 s, while the playroom sequence has a resolution of  $128 \times 128$  and spans 2.5 s. Each sequence provides events and ground truth poses for quantitative evaluation.

b) *Extended ESIM Simulations*: Given the relatively short duration and moderate motion patterns in the ECRot dataset, we generate additional sequences using ESIM to evaluate our method under more challenging conditions. These sequences are specifically designed to test:

- Various sequence durations (from 10 s to 80 s)
- Different angular velocities (from  $49.83^\circ/\text{s}$  to  $393.21^\circ/\text{s}$ )

c) *Real-World Sequences*: We collected ten real-world sequences using a synchronized setup consisting of an iNivation DVXplorer event camera ( $640 \times 480$  resolution) and a Livox Avia LiDAR. The two sensors are hardware-synchronized, and their extrinsic parameters are calibrated using the edge-based calibration method proposed in [57]. Ground truth camera trajectories are derived by combining high-precision LiDAR poses from Point-LIO [58] with the calibrated LiDAR-event camera extrinsic parameters, providing accurate benchmarks for evaluating our rotation estimation results.

3) *Hardware Configuration*: To ensure consistency and fair comparison across all experiments, we conducted our evaluations on a single laptop computer. The hardware configuration consists of an Intel Core i9-14900HX CPU, 32GB of RAM, and an NVIDIA RTX 4060 GPU.

## B. Experiments on ECRot Dataset

We conducted experiments using all six synthetic sequences from the ECRot dataset [38], comparing our method with several state-of-the-art approaches. Tab. III presents the quantitative results of our method compared to these approaches

including SMT [36], RTPT [37], CM-GAE [39], and CMax-SLAM [38].

Among all methods tested, none of them except CMax-SLAM and our EROAM demonstrated consistent performance. SMT, despite utilizing ground truth initialization to construct its initial map, fails to maintain stable pose estimation and quickly deviates from the initialized state, resulting in complete failure on all sequences. Moreover, SMT exhibits the highest computational overhead in our experiments. All other evaluated methods, including RTPT, CM-GAE, CMax-SLAM, and our EROAM, operate without requiring any prior pose information.

RTPT demonstrates better performance than SMT, maintaining tracking during initial camera rotations. However, it ultimately fails to process complete sequences despite multiple parameter tuning attempts, confirming the limitations reported in [38]. This failure occurs when the camera’s field of view (FOV) approaches the map boundaries - RTPT’s projection mechanism cannot effectively update the map in these situations, and attempts to increase the map size result in insufficient gradient information due to sparse projections.

CM-GAE showed inconsistent performance - we report its best results after multiple parameter tuning attempts, with successful processing of only the bicycle, town, and playroom sequences, though its performance remains unstable. These three methods demonstrate limited general applicability.

In contrast, both CMax-SLAM and our method successfully processed all six sequences. CMax-SLAM achieved this using their recommended sequence-specific parameters, while our method produced superior results using consistent parameters across all sequences, as evidenced by the lower  $\overline{ape}$  and  $\overline{rpe}$  values. We provide more detailed comparisons between CMax-SLAM and our method in IV-C and IV-E, where we evaluate performance under more challenging conditions and analyze computational efficiency.

To visualize the detailed performance differences, we present the rotation estimation results on the town sequence in Fig. 9. The figure shows both complete trajectories and zoomed-in views of roll, pitch, and yaw angles. SMT and RTPT quickly deviate from the ground truth and fail. CM-GAE maintains tracking but exhibits noticeable drift across all angles. In contrast, our method closely tracks the ground truth trajectory across all three rotation angles, with CMax-SLAM showing similar but slightly less accurate performance, particularly visible in the detailed views.

For qualitative evaluation, we focus on panoramic mapping results from CM-GAE, CMax-SLAM, and our method, as shown in Fig. 8. While CMax-SLAM’s original implementation generates panoramas at a fixed resolution of  $1024 \times 512$  (shown in Fig. 8b, with empty regions trimmed), our mapping framework operates in continuous spherical space rather than discrete panoramic space (detailed in III-F). This continuous representation enables panorama generation at arbitrary resolutions - for this comparison, we chose a resolution of  $7617 \times 2000$  to demonstrate the capability of our method.

To ensure fair visual comparison, we implement a unified panorama generation framework using each method’s estimated trajectories. Fig. 8a, Fig. 8c, and Fig. 8d show

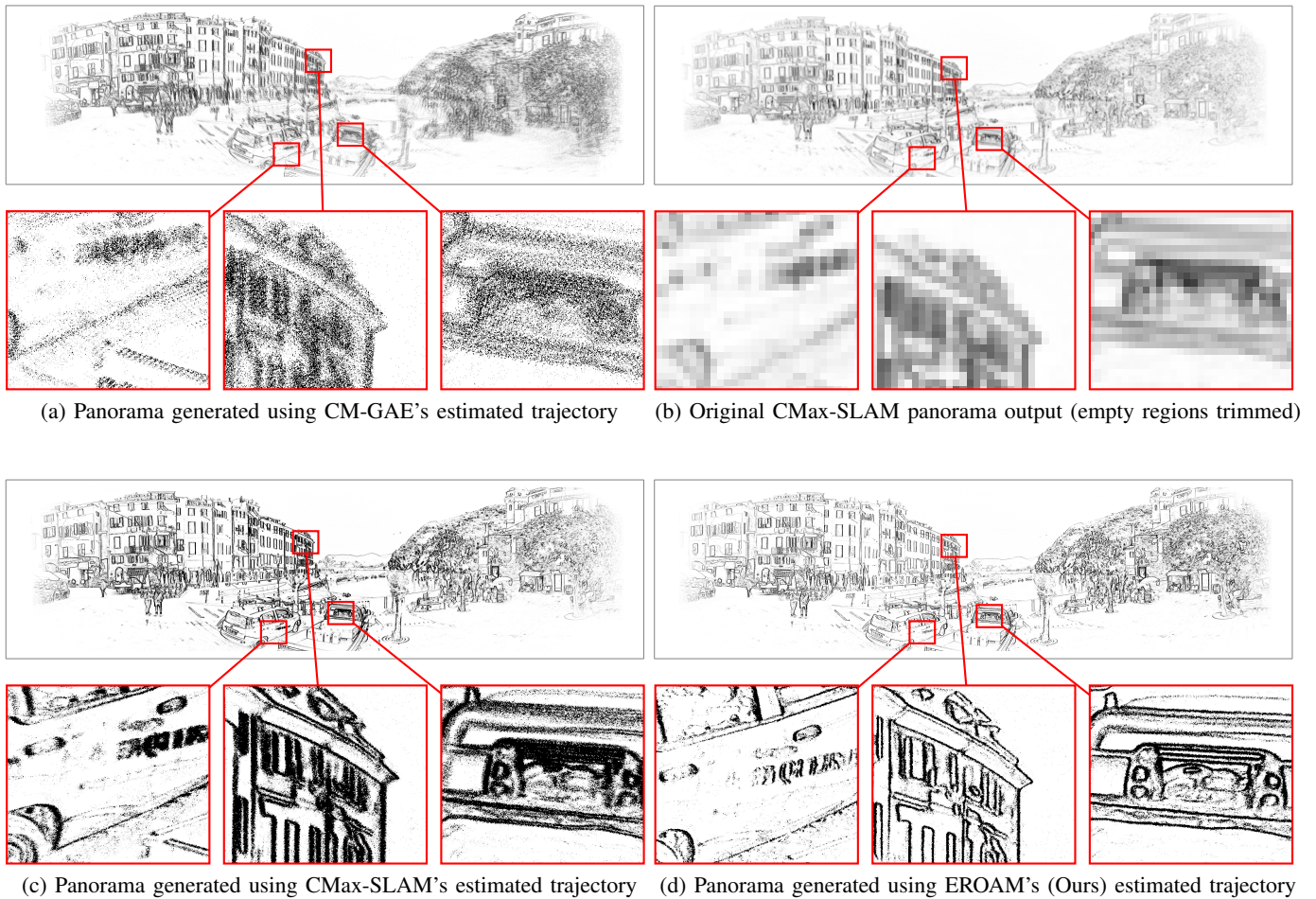


Fig. 8: Qualitative comparison of panoramic mapping results on the town sequence from ECRot dataset [38]. (a,c,d) show panoramas generated using our unified pipeline ( $7617 \times 2000$  resolution) with different methods’ estimated trajectories, where identical event window size (0.2 ms) and colorization scheme are applied. (b) shows the original panorama output from CMax-SLAM’s implementation for reference. The zoomed-in regions highlight that our method produces sharper edges and clearer structural details compared to other approaches.

TABLE III: Comparison of rotational motion estimation accuracy on ECRot [38] synthetic datasets.

Sequence	bay [38]		bicycle [38]		city [38]		street [38]		town [38]		playroom [38]	
	$\overline{ape}$ (°)	$\overline{rpe}$ (°)	$\overline{ape}$ (°)	$\overline{rpe}$ (°)	$\overline{ape}$ (°)	$\overline{rpe}$ (°)	$\overline{ape}$ (°)	$\overline{rpe}$ (°)	$\overline{ape}$ (°)	$\overline{rpe}$ (°)	$\overline{ape}$ (°)	$\overline{rpe}$ (°)
SMT [36]	-	-	-	-	-	-	-	-	-	-	-	-
RTPT [37]	-	-	-	-	-	-	-	-	-	-	-	-
CM-GAE [39]	-	-	0.856	0.244	-	-	-	-	2.60	0.603	3.684	0.823
CMax-SLAM [38]	0.802	0.141	0.727	0.098	1.113	0.294	0.517	0.181	1.238	0.130	0.727	<b>0.095</b>
EROAM (ours)	<b>0.163</b>	<b>0.045</b>	<b>0.107</b>	<b>0.039</b>	<b>0.101</b>	<b>0.044</b>	<b>0.116</b>	<b>0.047</b>	<b>0.142</b>	<b>0.045</b>	<b>0.384</b>	0.163

“-” indicates a failure case where after multiple attempts, the method still either produces  $\overline{ape}$  larger than  $20^\circ$ , crashes during execution, or outputs undefined quaternions.

panoramas generated using identical parameters: an event window size of 0.2 ms and consistent colorization scheme where the 90th percentile of event counts maps to intensity 255. All three methods’ panoramas are regenerated using their respective estimated trajectories through this unified pipeline.

As evident from the zoomed-in regions in Fig. 8, our method produces panoramic images with significantly sharper edges and clearer structural details compared to other approaches. The improved quality is particularly noticeable in architectural features and text regions, demonstrating the benefits of our accurate rotation estimation.

### C. Extended Simulation Analysis

While both CMax-SLAM and EROAM successfully process all ECRot sequences, these sequences are short (5s) and exhibit moderate motion patterns, as shown in Fig. 9. For reference, the ECRot-bicycle sequence has an average angular velocity of  $84.13^\circ/\text{s}$  and acceleration of  $101.73^\circ/\text{s}^2$ . To evaluate the generality and robustness of our method, we conducted extended simulation experiments using ESIM [56] with the bicycle scene from ECRot dataset under more challenging conditions.

As shown in Fig. 10a, we designed two sets of sequences

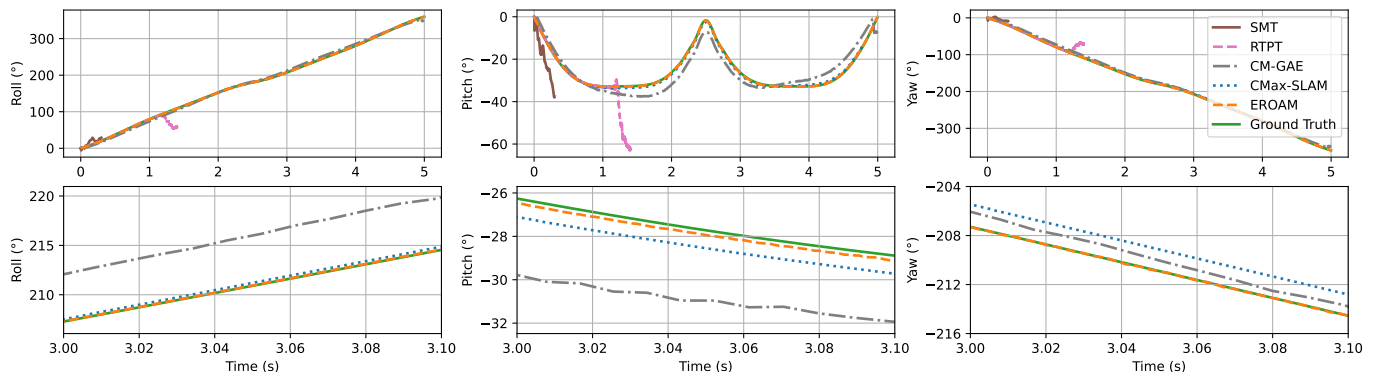


Fig. 9: Rotation estimation results on the town sequence from ECRot dataset. The top row shows the full trajectories of roll, pitch, and yaw angles, while the bottom row shows the zoomed-in views from 3.00 s to 3.10 s. Our method (EROAM) achieves comparable accuracy with the ground truth, demonstrating robust rotation estimation performance. The trajectories of SMT and RTPT are truncated after significant deviation from ground truth for better visualization clarity.

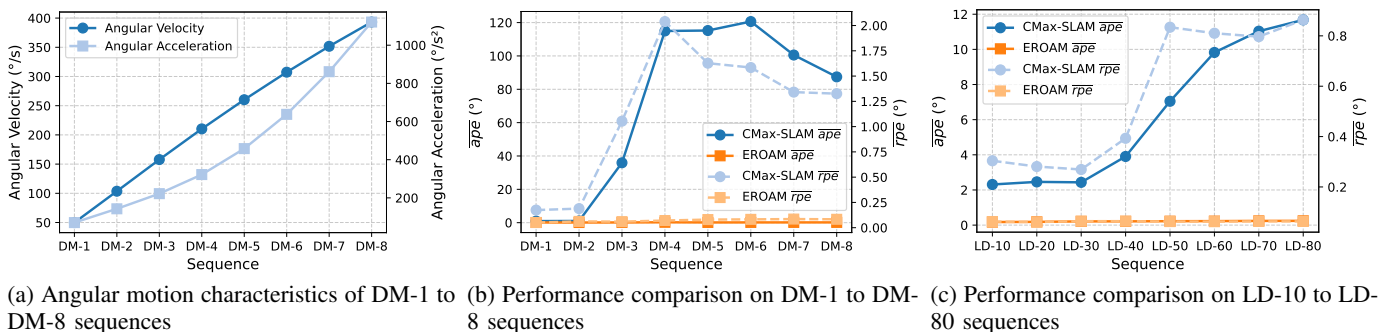


Fig. 10: Quantitative evaluation results. (a) Shows the angular velocity ( $49.83^\circ/\text{s}$  to  $393.21^\circ/\text{s}$ ) and acceleration ( $70.41^\circ/\text{s}^2$  to  $1121.32^\circ/\text{s}^2$ ) characteristics of DM-1 to DM-8 sequences (each 5 s long). (b) Compares the  $\overline{ape}$  and  $\overline{rpe}$  metrics across DM-1 to DM-8 sequences with increasing angular velocities. (c) Compares the  $\overline{ape}$  and  $\overline{rpe}$  metrics for LD-10 to LD-80 sequences of increasing durations (10 s to 80 s).

TABLE IV: Quantitative comparison of rotational state estimation under increasing angular velocities.

Sequence	DM-1		DM-2		DM-3		DM-4		DM-5		DM-6		DM-7		DM-8	
	$\overline{ape}$ (°)	$\overline{rpe}$ (°)	$\overline{ape}$ (°)	$\overline{rpe}$ (°)	$\overline{ape}$ (°)	$\overline{rpe}$ (°)	$\overline{ape}$ (°)	$\overline{rpe}$ (°)	$\overline{ape}$ (°)	$\overline{rpe}$ (°)	$\overline{ape}$ (°)	$\overline{rpe}$ (°)	$\overline{ape}$ (°)	$\overline{rpe}$ (°)	$\overline{ape}$ (°)	$\overline{rpe}$ (°)
CMax-SLAM [38]	0.947	0.174	1.032	0.189	35.927	1.054	114.962	2.040	115.238	1.627	120.625	1.585	100.548	1.341	87.440	1.326
EROAM (ours)	<b>0.116</b>	<b>0.051</b>	<b>0.105</b>	<b>0.062</b>	<b>0.138</b>	<b>0.060</b>	<b>0.236</b>	<b>0.071</b>	<b>0.142</b>	<b>0.080</b>	<b>0.162</b>	<b>0.082</b>	<b>0.164</b>	<b>0.085</b>	<b>0.176</b>	<b>0.083</b>

TABLE V: Assessment of long-term estimation stability across sequences of increasing duration.

Sequence	LD-10		LD-20		LD-30		LD-40		LD-50		LD-60		LD-70		LD-80	
	$\overline{ape}$ (°)	$\overline{rpe}$ (°)	$\overline{ape}$ (°)	$\overline{rpe}$ (°)	$\overline{ape}$ (°)	$\overline{rpe}$ (°)	$\overline{ape}$ (°)	$\overline{rpe}$ (°)	$\overline{ape}$ (°)	$\overline{rpe}$ (°)	$\overline{ape}$ (°)	$\overline{rpe}$ (°)	$\overline{ape}$ (°)	$\overline{rpe}$ (°)	$\overline{ape}$ (°)	$\overline{rpe}$ (°)
CMax-SLAM [38]	2.312	0.304	2.460	0.281	2.434	0.269	3.905	0.393	7.047	0.834	9.824	0.810	11.033	0.797	11.677	0.863
EROAM (ours)	<b>0.175</b>	<b>0.062</b>	<b>0.185</b>	<b>0.061</b>	<b>0.212</b>	<b>0.064</b>	<b>0.214</b>	<b>0.064</b>	<b>0.223</b>	<b>0.063</b>	<b>0.227</b>	<b>0.062</b>	<b>0.239</b>	<b>0.063</b>	<b>0.242</b>	<b>0.063</b>

to test different aspects: (1) sequences with increasing angular velocities and accelerations (DM-1 through DM-8), and (2) sequences of increasing duration (LD-10 through LD-80). For the dynamic motion sequences, we progressively increased the magnitude and frequency of rotational motion while maintaining the 5s duration, with angular velocity ranging from  $49.83^\circ/\text{s}$  to  $393.21^\circ/\text{s}$  and angular acceleration from  $70.41^\circ/\text{s}^2$  to  $1121.32^\circ/\text{s}^2$ . For the duration test sequences, we used a moderate dynamic profile (average angular velocity:  $107.24^\circ/\text{s}$ , average angular acceleration:  $200.93^\circ/\text{s}^2$ ) and varied the sequence length from 10s to 80s.

Tab. IV and Fig. 10b present the performance comparison under different angular velocities. While both methods per-

form well under moderate motion (DM-1 and DM-2,  $\overline{ape} \leq 1.032^\circ$ ), CMax-SLAM's performance degrades significantly when angular velocity increases (DM-3 onwards), with  $\overline{ape}$  exceeding  $100^\circ$  in high-velocity scenarios. This degradation stems from a fundamental limitation of the contrast maximization framework: it assumes constant angular velocity within each time window used for estimation. Under high-dynamic motions with large angular accelerations, this assumption becomes invalid, leading to significant estimation errors. Although CMax-SLAM employs backend optimization, it cannot recover from these fundamental front-end estimation errors. This is clearly demonstrated in Fig. 12, where CMax-SLAM's panoramic reconstruction shows severe ghosting artifacts and

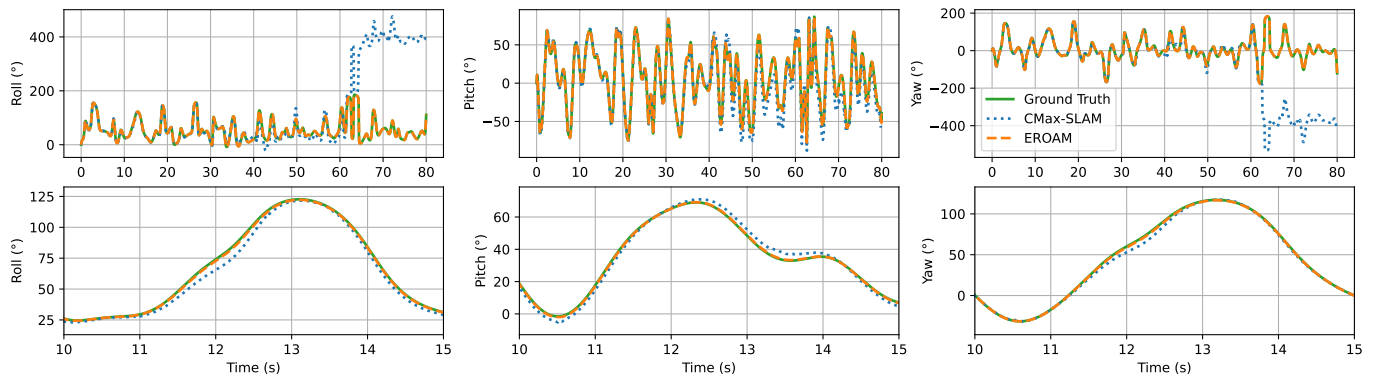
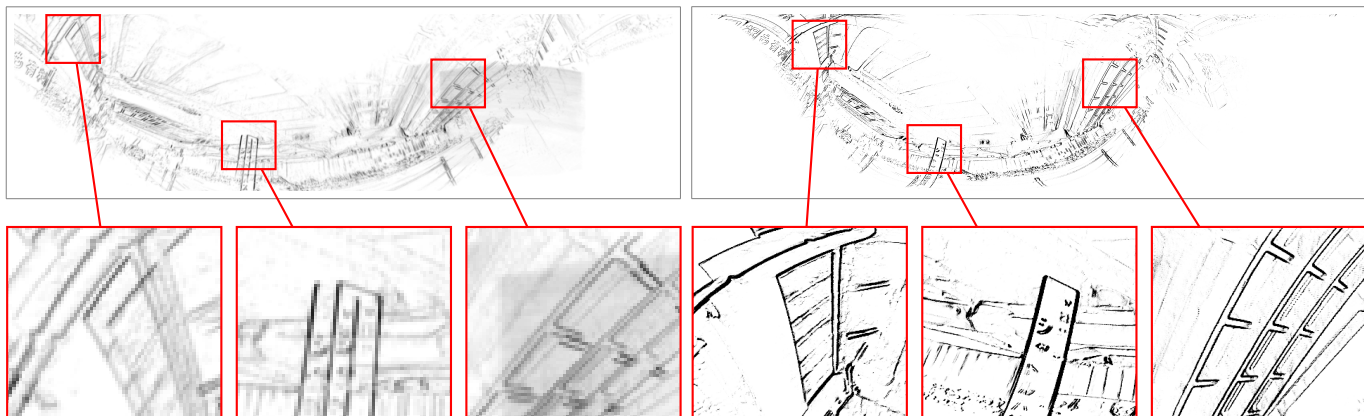


Fig. 11: Comparison of rotational state estimation on the LD-80 sequence. The top row shows the complete 80s trajectories for roll, pitch, and yaw angles, where CMax-SLAM exhibits significant consistency issues and deviates from ground truth starting from 40s. The bottom row presents detailed views between 10s and 15s, revealing that CMax-SLAM’s estimation already shows noticeable errors even in this early stage. In contrast, EROAM maintains consistent accuracy throughout the entire sequence, closely aligning with ground truth in both global and local perspectives.



(a) Panoramic image from CMax-SLAM (original  $1024 \times 512$  resolution, empty regions trimmed) (b) Panoramic image from EROAM (Ours,  $5441 \times 1000$  resolution)

Fig. 12: Qualitative comparison of panoramic mapping results on the DM-4 sequence with high angular velocity. CMax-SLAM’s result exhibits significant ghosting artifacts and double edges in structures, indicating severe rotation estimation errors under high-dynamic motion. These artifacts are particularly visible in the zoomed-in regions, where single structures appear multiple times due to inconsistent motion estimates. In contrast, EROAM produces a high-resolution panorama with sharp details and precisely aligned structures, demonstrating accurate rotation estimation throughout the sequence.

double edges due to incorrect motion estimation under high angular velocities.

The comparison across different sequence durations, shown in Tab. V and Fig. 10c, reveals similar patterns. CMax-SLAM exhibits increasing drift as sequence length grows, with  $\overline{ape}$  rising from  $2.312^\circ$  in LD-10 to  $11.677^\circ$  in LD-80. This drift accumulation is clearly visualized in Fig. 11, where CMax-SLAM’s estimated trajectory shows significant deviation from ground truth, particularly after 40s. This further demonstrates how initial estimation errors in the contrast maximization framework propagate over time, despite backend optimization attempts. In contrast, our method maintains consistent accuracy across all sequences ( $\overline{ape} \leq 0.242^\circ$ ,  $\overline{rpe} \approx 0.063^\circ$ ), as our ES-ICP approach directly optimizes geometric constraints on the unit sphere without relying on assumptions about constant angular velocity.

These results demonstrate that our method not only achieves

higher accuracy but also maintains consistent performance under challenging conditions where CMax-SLAM struggles, suggesting superior robustness and general applicability.

#### D. Experiments on Real-World Data

To validate our method’s performance in real-world scenarios, we collected and evaluated EROAM on our EROAM-campus dataset. The dataset contains ten sequences captured using a custom-built synchronized sensor suite, consisting of an iniVation DVXplorer event camera ( $640 \times 480$  resolution) and a Livox Avia LiDAR mounted on a tripod. Both sensors were hardware-synchronized, and their extrinsic parameters were calibrated using the edge-based calibration method proposed in [57], [59]. We manually performed arbitrary 3-DoF rotational motions while recording data, and obtained ground truth camera trajectories by combining high-precision LiDAR

TABLE VI: Comparison of rotational motion estimation accuracy on EROAM-campus datasets.

Sequence	canteen-entrance		distant-building		embankment-360		embankment		lawn-360	
	$\overline{ape}$ ( $^\circ$ )	$\overline{rpe}$ ( $^\circ$ )	$\overline{ape}$ ( $^\circ$ )	$\overline{rpe}$ ( $^\circ$ )	$\overline{ape}$ ( $^\circ$ )	$\overline{rpe}$ ( $^\circ$ )	$\overline{ape}$ ( $^\circ$ )	$\overline{rpe}$ ( $^\circ$ )	$\overline{ape}$ ( $^\circ$ )	$\overline{rpe}$ ( $^\circ$ )
SMT [36]	-	-	-	-	-	-	-	-	-	-
RTPT [37]	-	-	-	-	-	-	0.654	0.403	-	-
CM-GAE [39]	0.688	0.371	5.915	0.899	4.727	0.729	3.228	0.424	7.776	0.670
CMax-SLAM [38]	0.662	0.557	5.958	1.312	-	-	4.658	2.298	8.733	0.691
<b>EROAM (ours)</b>	<b>0.312</b>	<b>0.278</b>	<b>0.285</b>	<b>0.243</b>	<b>1.557</b>	<b>0.537</b>	<b>0.413</b>	<b>0.224</b>	<b>1.221</b>	<b>0.415</b>

Sequence	lawn		lecture-hall		front-gate		rooftop		window-building	
	$\overline{ape}$ ( $^\circ$ )	$\overline{rpe}$ ( $^\circ$ )	$\overline{ape}$ ( $^\circ$ )	$\overline{rpe}$ ( $^\circ$ )	$\overline{ape}$ ( $^\circ$ )	$\overline{rpe}$ ( $^\circ$ )	$\overline{ape}$ ( $^\circ$ )	$\overline{rpe}$ ( $^\circ$ )	$\overline{ape}$ ( $^\circ$ )	$\overline{rpe}$ ( $^\circ$ )
SMT [36]	-	-	-	-	-	-	-	-	-	-
RTPT [37]	-	-	-	-	-	-	-	-	-	-
CM-GAE [39]	-	-	3.103	0.407	-	-	14.063	0.695	10.954	1.227
CMax-SLAM [38]	-	-	0.518	0.457	13.549	1.227	0.841	0.406	8.201	4.698
<b>EROAM (ours)</b>	<b>0.405</b>	<b>0.226</b>	<b>0.246</b>	<b>0.222</b>	<b>0.473</b>	<b>0.305</b>	<b>0.655</b>	<b>0.237</b>	<b>0.229</b>	<b>0.184</b>

“-” indicates a failure case where after multiple attempts, the method still either produces  $\overline{ape}$  larger than  $20^\circ$ , crashes during execution, or outputs undefined quaternions.

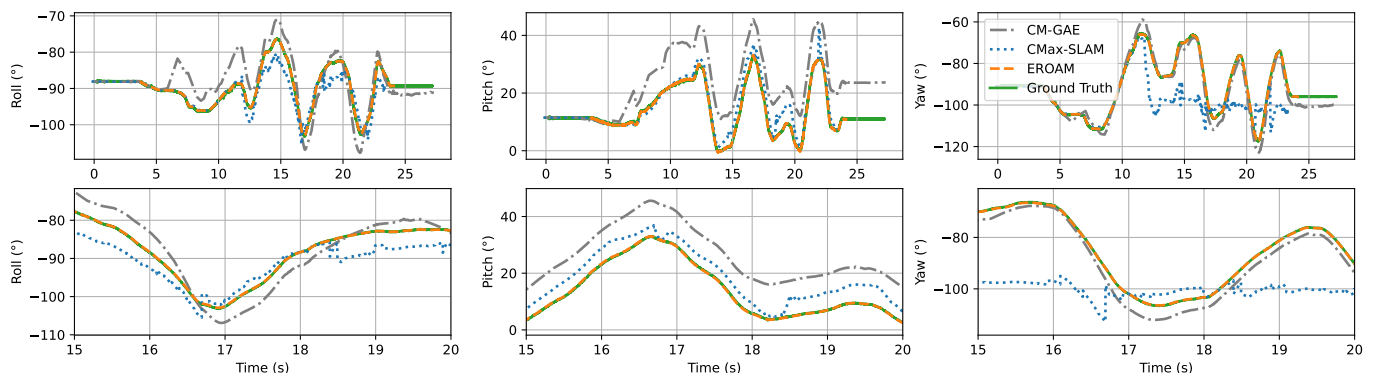


Fig. 13: Comparison of rotational state estimation on the window-building sequence. The top row shows the complete trajectories for roll, pitch, and yaw angles, while the bottom row presents detailed views between 15 s and 20 s. Our method (EROAM) maintains accurate tracking throughout the sequence, closely following the ground truth trajectory, while CM-GAE and CMax-SLAM show noticeable deviations, particularly evident in the zoomed-in views.

poses from Point-LIO [58] with the calibrated LiDAR-event camera extrinsic parameters.

The quantitative comparison results across all sequences are presented in Tab. VI. SMT fails to process any of the sequences, despite multiple parameter tuning attempts. RTPT shows very limited success, only managing to process the embankment sequence with an  $\overline{ape}$  of  $0.654^\circ$ , but failing on all other sequences. CM-GAE and CMax-SLAM show inconsistent performance across different sequences - CM-GAE successfully processes 7 out of 10 sequences while CMax-SLAM processes 6, with both methods exhibiting significantly higher errors compared to our method when they do succeed, with  $\overline{ape}$  ranging from  $0.518^\circ$  to  $14.063^\circ$ .

In contrast, EROAM successfully processes all sequences while maintaining superior accuracy. Our method achieves the lowest error rates across all sequences, with  $\overline{ape}$  consistently below  $1.557^\circ$  and  $\overline{rpe}$  below  $0.537^\circ$ . The most challenging sequence is embankment-360, where EROAM still maintains reasonable accuracy ( $\overline{ape} = 1.557^\circ$ ) while CMax-SLAM fails completely.

The superior accuracy of our method is particularly evident in the window-building sequence, as shown in Fig. 13. While

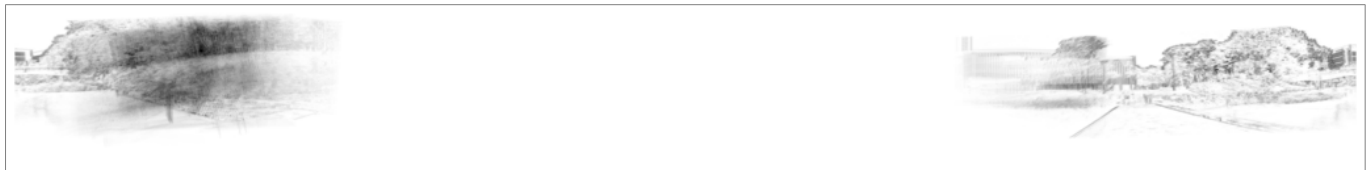
both CM-GAE and CMax-SLAM exhibit significant drift and inconsistent estimation across all three rotation angles, EROAM closely tracks the ground truth trajectory throughout the sequence. The detailed views between 15 s and 20 s clearly demonstrate our method’s ability to maintain accurate rotation estimation even during complex motion patterns.

This accuracy in rotation estimation directly translates to high-quality panoramic reconstruction results. As shown in Fig. 14, EROAM produces significantly clearer panoramas compared to CMax-SLAM. The comparison between the front-gate sequence results demonstrates our method’s superior performance in maintaining structural clarity and avoiding ghosting artifacts. This advantage is further emphasized in the embankment-360 sequence, where EROAM successfully reconstructs a complete  $360^\circ$  panorama with consistent quality.

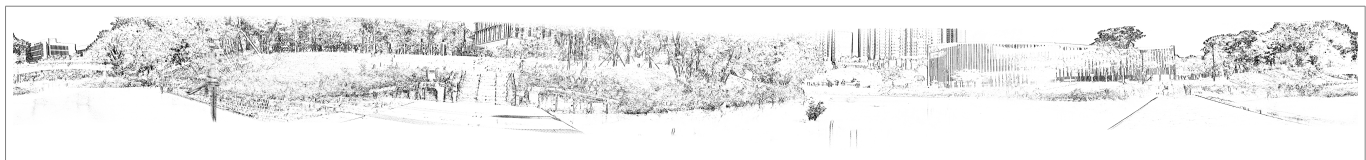
To demonstrate our method’s versatility across different environments, we present additional reconstruction results in Fig. 15. These results showcase EROAM’s ability to handle various scene structures while maintaining high reconstruction quality. The zoomed-in regions highlight the preservation of fine details across different sequences including distant-building, lecture-hall, rooftop and window-building.



(a) CMax-SLAM result on front-gate sequence ( $1024 \times 512$  resolution, empty regions trimmed), (b) EROAM result on front-gate sequence ( $2769 \times 1000$  resolution, empty regions trimmed)



(c) CMax-SLAM result on embankment-360 sequence ( $1024 \times 512$  resolution, empty regions trimmed)



(d) EROAM result on embankment-360 sequence ( $9668 \times 1000$  resolution)

Fig. 14: Qualitative comparison of panoramic mapping results on real-world sequences. The zoomed-in regions in (a,b) highlight the superior structural clarity achieved by our method compared to CMax-SLAM’s results with ghosting artifacts. The full  $360^\circ$  panoramas in (c,d) demonstrate EROAM’s ability to maintain consistent reconstruction quality across extended views.

TABLE VII: Runtime comparison on ECRot sequences.

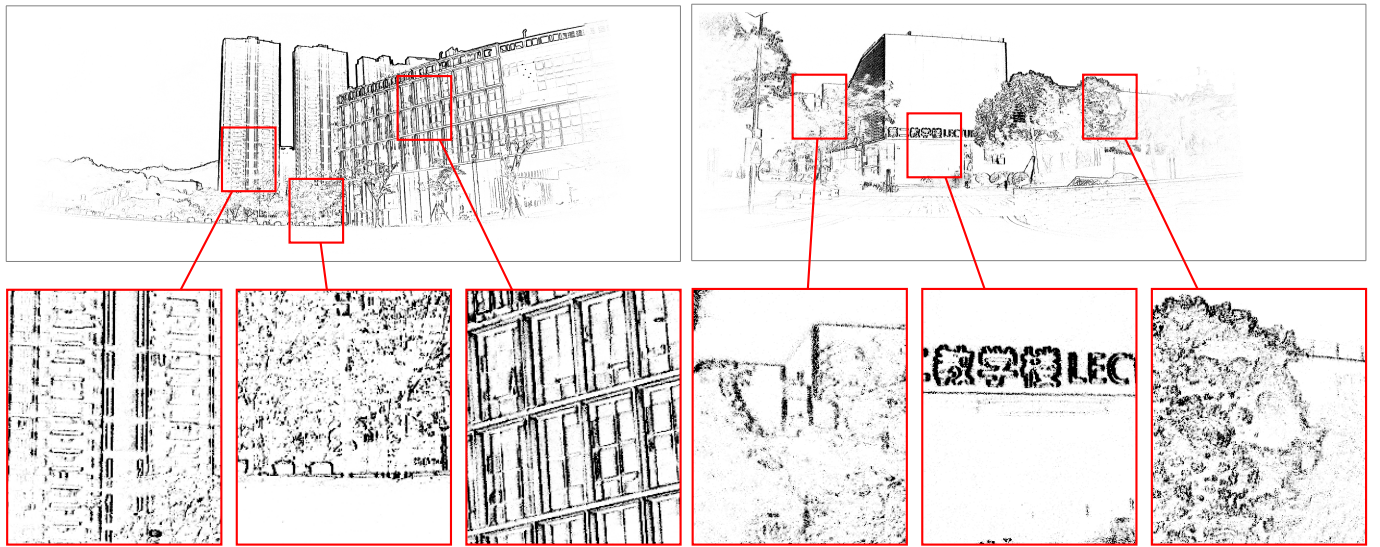
Sequence	Duration (s)	Runtime (seconds)			
		RTPT [37]	CM-GAE* [39]	CMax-SLAM [38]	EROAM (ours)
bay	5.000	67.245	114.744	262.272	<b>5.931</b>
bicycle	5.000	35.620	9.283	63.632	<b>5.858</b>
city	5.000	79.172	151.906	336.170	<b>6.092</b>
street	5.000	56.532	117.441	197.090	<b>5.704</b>
town	5.000	62.541	68.969	194.032	<b>5.927</b>
playroom	2.500	3.785	<b>2.423</b>	18.987	2.499

### E. Runtime Analysis

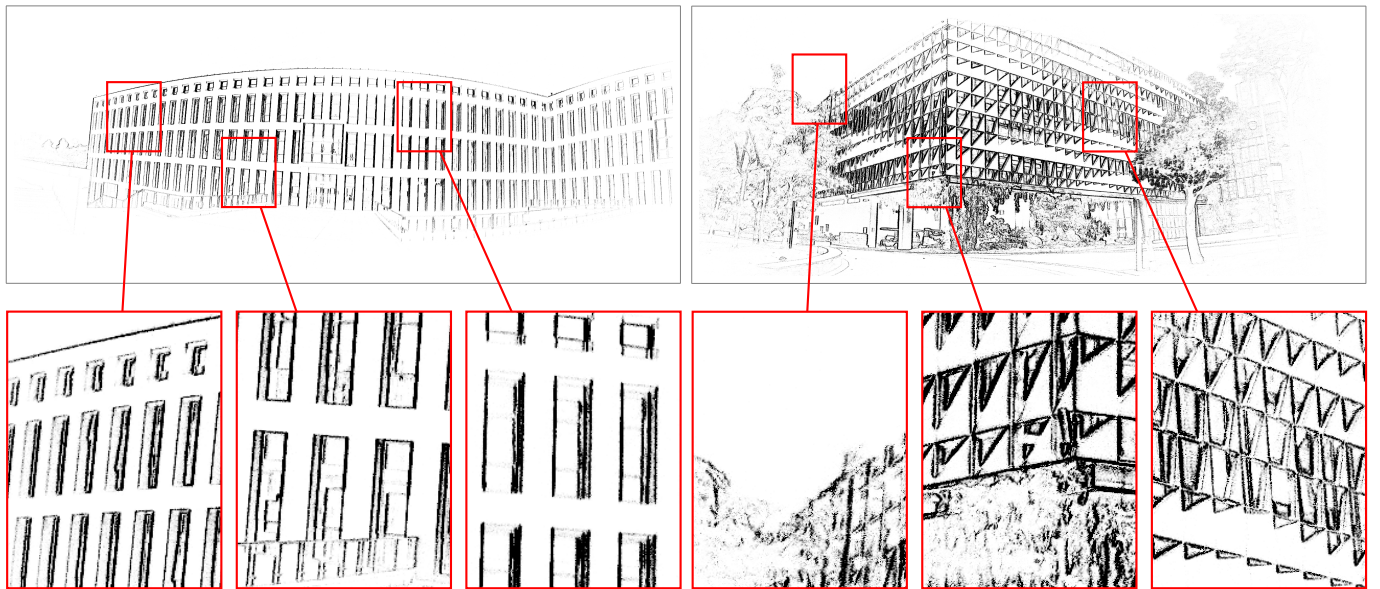
Tab. VII and Tab. VIII present the runtime comparison of RTPT, CM-GAE, CMax-SLAM, and our EROAM method on both synthetic ECRot sequences and real-world EROAM-campus sequences. Note that SMT is excluded from the comparison as it fails to process any sequences successfully and exhibits prohibitively high computational costs even during failed attempts. All experiments were conducted on a laptop

with an Intel Core i9-14900HX CPU and 32GB RAM, with RTPT utilizing an NVIDIA RTX 4060 GPU while all other methods run on CPU only.

Our implementation adapts to different dataset characteristics: for ECRot sequences ( $240 \times 180$  resolution), EROAM estimates rotation at  $f = 1000$  Hz, while for EROAM-campus sequences captured with a higher resolution camera ( $640 \times 480$ ) generating significantly more events, we adjust to



(a) EROAM result on distant-building sequence ( $5441 \times 1000$  resolution) (b) EROAM result on lecture-hall sequence ( $3517 \times 1000$  resolution, empty regions trimmed)



(c) EROAM result on rooftop sequence ( $6873 \times 1000$  resolution, empty regions trimmed) (d) EROAM result on window-building sequence ( $4129 \times 1000$  resolution)

Fig. 15: Additional visualization results from EROAM on different sequences. Each panorama demonstrates high-quality reconstruction with precise structure alignment and sharp details, as highlighted in the zoomed-in regions. These results showcase EROAM’s consistent performance across various challenging scenarios with different motion patterns and scene structures.

$f = 200$  Hz to balance computational load while maintaining tracking accuracy.

EROAM demonstrates superior computational efficiency across both datasets. For synthetic data, our method processes most sequences in approximately 6s. On real-world data, taking the 31.413s embankment sequence as an example, EROAM achieves remarkable speedups:  $6.2\times$  compared to CM-GAE,  $5.3\times$  compared to RTPT (despite its GPU acceleration), and  $17.6\times$  compared to CMax-SLAM. CMax-SLAM’s performance degrades significantly with sequence duration due to its combination of contrast maximization and backend

optimization, with processing time scaling poorly with event density. CM-GAE exhibits similar limitations. EROAM, in contrast, achieves real-time performance even for extended sequences - processing the 47.165s lawn sequence in 47.168s, while other methods require substantially longer: CM-GAE takes 1318.581s and CMax-SLAM needs 2553.260s.

This consistent performance stems from two key design choices. First, our spherical map representation significantly simplifies map maintenance. Unlike RTPT’s complex map updates and feature management operations, EROAM simply appends new keyframe point clouds to the spherical surface,

TABLE VIII: Runtime comparison on EROAM-campus sequences.

Sequence	Duration (s)	Runtime (seconds)			
		RTPT* [37]	CM-GAE [39]	CMax-SLAM [38]	EROAM (ours)
canteen-entrance	19.587	200.557	441.424	520.178	<b>19.594</b>
distant-building	29.193	97.019	191.737	386.502	<b>29.214</b>
embankment	31.413	166.443	196.604	552.528	<b>31.459</b>
embankment-360	18.100	174.606	181.257	782.102	<b>18.134</b>
lawn	47.165	-	1318.581	2553.260	<b>47.168</b>
lawn-360	16.085	226.574	347.039	558.310	<b>16.094</b>
lecture-hall	18.365	99.170	915.236	256.658	<b>18.373</b>
front-gate	26.149	294.268	270.939	794.393	<b>26.154</b>
rooftop	50.263	321.165	410.770	845.354	<b>50.344</b>
window-building	27.510	335.886	877.523	1417.175	<b>27.514</b>

\*RTPT fails to process the lawn sequence due to its large size.

substantially reducing computational overhead.

Second, our ES-ICP algorithm fundamentally avoids the computational bottlenecks inherent in contrast maximization-based methods. While CM-GAE and CMax-SLAM require iterative contrast computation over event time windows and computationally intensive event warping operations after each velocity update, EROAM’s ES-ICP solution:

- Eliminates repeated event warping requirements
- Enables parallel processing of point-to-line distances and their Jacobians across CPU cores
- Maintains consistent computational load regardless of event rate or scene complexity

The experimental results clearly demonstrate EROAM’s superior computational efficiency and scalability. By maintaining real-time performance across both synthetic and real-world scenarios while requiring only CPU resources, EROAM presents a practical solution for event-based rotational motion estimation in real-world applications.

## V. CONCLUSION

In this paper, we have introduced EROAM, a novel approach to event-based rotational motion estimation. Our method advances the state of the art through several key innovations. First, we propose a spherical representation that simplifies rotational motion formulation while enabling continuous mapping. Second, we develop an Event Spherical ICP algorithm that efficiently processes events in parallel while maintaining high accuracy. Third, we present a real-time implementation that achieves superior performance. Through extensive evaluation on both synthetic and real-world datasets, we have demonstrated EROAM’s robust performance across various challenging conditions, including high angular velocities and extended sequences. The success of our ICP-based approach suggests promising potential for broader applications in event camera tasks, offering significant advantages in both computational efficiency and accuracy compared to existing contrast maximization frameworks.

## REFERENCES

- [1] D. Martinec and T. Pajdla, “Robust rotation and translation estimation in multiview reconstruction,” in *2007 IEEE conference on computer vision and pattern recognition*. IEEE, 2007, pp. 1–8.
- [2] P. Lichtsteiner, C. Posch, and T. Delbruck, “A 128×128 120 db 15 $\mu$ s latency asynchronous temporal contrast vision sensor,” *IEEE journal of solid-state circuits*, vol. 43, no. 2, pp. 566–576, 2008.
- [3] C. Brandli, R. Berner, M. Yang, S.-C. Liu, and T. Delbruck, “A 240×180 130 db 3  $\mu$ s latency global shutter spatiotemporal vision sensor,” *IEEE Journal of Solid-State Circuits*, vol. 49, no. 10, pp. 2333–2341, 2014.
- [4] G. Gallego, T. Delbrück, G. Orchard, C. Bartolozzi, B. Taba, A. Censi, S. Leutenegger, A. J. Davison, J. Conradt, K. Daniilidis *et al.*, “Event-based vision: A survey,” *IEEE transactions on pattern analysis and machine intelligence*, vol. 44, no. 1, pp. 154–180, 2020.
- [5] G. Gallego and D. Scaramuzza, “Accurate angular velocity estimation with an event camera,” *IEEE Robotics and Automation Letters*, vol. 2, no. 2, pp. 632–639, 2017.
- [6] J. Niu, S. Zhong, X. Lu, S. Shen, G. Gallego, and Y. Zhou, “Esvo2: Direct visual-inertial odometry with stereo event cameras,” *arXiv preprint arXiv:2410.09374*, 2024.
- [7] L. Gao, Y. Liang, J. Yang, S. Wu, C. Wang, J. Chen, and L. Kneip, “Vector: A versatile event-centric benchmark for multi-sensor slam,” *IEEE Robotics and Automation Letters*, vol. 7, no. 3, pp. 8217–8224, 2022.
- [8] W. Chamorro, J. Solà, and J. Andrade-Cetto, “Event-based line slam in real-time,” *IEEE Robotics and Automation Letters*, vol. 7, no. 3, pp. 8146–8153, 2022.
- [9] A. R. Vidal, H. Rebecq, T. Horstschaefer, and D. Scaramuzza, “Ultimate slam? combining events, images, and imu for robust visual slam in hdr and high-speed scenarios,” *IEEE Robotics and Automation Letters*, vol. 3, no. 2, pp. 994–1001, 2018.
- [10] S. Lin, Y. Zhang, D. Huang, B. Zhou, X. Luo, and J. Pan, “Fast event-based double integral for real-time robotics,” in *2023 IEEE International Conference on Robotics and Automation (ICRA)*. IEEE, 2023, pp. 796–803.
- [11] D. Qu, C. Yan, D. Wang, J. Yin, Q. Chen, D. Xu, Y. Zhang, B. Zhao, and X. Li, “Implicit event-rgbd neural slam,” in *Proceedings of the IEEE/CVF Conference on Computer Vision and Pattern Recognition*, 2024, pp. 19 584–19 594.
- [12] S. Sun, G. Cioffi, C. De Visser, and D. Scaramuzza, “Autonomous quadrotor flight despite rotor failure with onboard vision sensors: Frames vs. events,” *IEEE Robotics and Automation Letters*, vol. 6, no. 2, pp. 580–587, 2021.
- [13] D. Falanga, K. Kleber, and D. Scaramuzza, “Dynamic obstacle avoidance for quadrotors with event cameras,” *Science Robotics*, vol. 5, no. 40, p. eaaz9712, 2020.
- [14] C. Iaboni, H. Patel, D. Lobo, J.-W. Choi, and P. Abichandani, “Event camera based real-time detection and tracking of indoor ground robots,” *IEEE Access*, vol. 9, pp. 166 588–166 602, 2021.
- [15] A. Bhattacharya, M. Cannici, N. Rao, Y. Tao, V. Kumar, N. Matni, and D. Scaramuzza, “Monocular event-based vision for obstacle avoidance with a quadrotor,” *arXiv preprint arXiv:2411.03303*, 2024.
- [16] S. Afshar, N. Ralph, Y. Xu, J. Tapson, A. v. Schaik, and G. Cohen, “Event-based feature extraction using adaptive selection thresholds,” *Sensors*, vol. 20, no. 6, p. 1600, 2020.
- [17] H. Seok and J. Lim, “Robust feature tracking in dvs winter stream using bézier mapping,” in *Proceedings of the IEEE/CVF Winter Conference on Applications of Computer Vision*, 2020, pp. 1658–1667.
- [18] Z. Huang, L. Sun, C. Zhao, S. Li, and S. Su, “Eventpoint: Self-supervised interest point detection and description for event-based camera,” in *Proceedings of the IEEE/CVF Winter Conference on Applications of Computer Vision*, 2023, pp. 5396–5405.
- [19] S. Lin, F. Xu, X. Wang, W. Yang, and L. Yu, “Efficient spatial-temporal normalization of sae representation for event camera,” *IEEE Robotics and Automation Letters*, vol. 5, no. 3, pp. 4265–4272, 2020.



- [20] S. Shiba, Y. Aoki, and G. Gallego, "Fast event-based optical flow estimation by triplet matching," *IEEE Signal Processing Letters*, vol. 29, pp. 2712–2716, 2022.
- [21] M. Gehrig, M. Millhäusler, D. Gehrig, and D. Scaramuzza, "E-raft: Dense optical flow from event cameras," in *2021 International Conference on 3D Vision (3DV)*. IEEE, 2021, pp. 197–206.
- [22] S. Shiba, Y. Aoki, and G. Gallego, "Secrets of event-based optical flow," in *European Conference on Computer Vision*. Springer, 2022, pp. 628–645.
- [23] C. Lee, A. K. Kosta, A. Z. Zhu, K. Chaney, K. Daniilidis, and K. Roy, "Spike-flownet: event-based optical flow estimation with energy-efficient hybrid neural networks," in *European Conference on Computer Vision*. Springer, 2020, pp. 366–382.
- [24] C. Scheerlinck, H. Rebecq, D. Gehrig, N. Barnes, R. Mahony, and D. Scaramuzza, "Fast image reconstruction with an event camera," in *Proceedings of the IEEE/CVF Winter Conference on Applications of Computer Vision*, 2020, pp. 156–163.
- [25] H. Rebecq, R. Ranftl, V. Koltun, and D. Scaramuzza, "Events-to-video: Bringing modern computer vision to event cameras," in *Proceedings of the IEEE/CVF Conference on Computer Vision and Pattern Recognition*, 2019, pp. 3857–3866.
- [26] —, "High speed and high dynamic range video with an event camera," *IEEE transactions on pattern analysis and machine intelligence*, vol. 43, no. 6, pp. 1964–1980, 2019.
- [27] S. Klenk, L. Koestler, D. Scaramuzza, and D. Cremers, "E-nerf: Neural radiance fields from a moving event camera," *IEEE Robotics and Automation Letters*, vol. 8, no. 3, pp. 1587–1594, 2023.
- [28] I. Hwang, J. Kim, and Y. M. Kim, "Ev-nerf: Event based neural radiance field," in *Proceedings of the IEEE/CVF Winter Conference on Applications of Computer Vision*, 2023, pp. 837–847.
- [29] V. Rudnev, M. Elgharib, C. Theobalt, and V. Golyanik, "Eventnerf: Neural radiance fields from a single colour event camera," in *Proceedings of the IEEE/CVF Conference on Computer Vision and Pattern Recognition*, 2023, pp. 4992–5002.
- [30] Y. Xue, H. Li, S. Leutenegger, and J. Stückler, "Event-based non-rigid reconstruction of low-rank parametrized deformations from contours," *International Journal of Computer Vision*, pp. 1–19, 2024.
- [31] S. Lin, Y. Zhang, L. Yu, B. Zhou, X. Luo, and J. Pan, "Autofocus for event cameras," in *Proceedings of the IEEE/CVF Conference on Computer Vision and Pattern Recognition*, 2022, pp. 16344–16353.
- [32] W. Liao, X. Zhang, L. Yu, S. Lin, W. Yang, and N. Qiao, "Synthetic aperture imaging with events and frames," in *Proceedings of the IEEE/CVF Conference on Computer Vision and Pattern Recognition*, 2022, pp. 17735–17744.
- [33] B. He, Z. Wang, Y. Zhou, J. Chen, C. D. Singh, H. Li, Y. Gao, S. Shen, K. Wang, Y. Cao *et al.*, "Microsaccade-inspired event camera for robotics," *Science Robotics*, vol. 9, no. 90, p. eadj8124, 2024.
- [34] S. Lin, X. Zhang, L. Yang, L. Yu, B. Zhou, X. Luo, W. Wang, and J. Pan, "Neuromorphic synergy for video binarization," *IEEE Transactions on Image Processing*, 2024.
- [35] T. Finateu, A. Niwa, D. Matolin, K. Tsuchimoto, A. Mascheroni, E. Reynaud, P. Mostafalu, F. Brady, L. Chotard, F. LeGoff *et al.*, "5.10 a 1280× 720 back-illuminated stacked temporal contrast event-based vision sensor with 4.86  $\mu\text{m}$  pixels, 1.066 gepps readout, programmable event-rate controller and compressive data-formatting pipeline," in *2020 IEEE International Solid-State Circuits Conference-(ISSCC)*. IEEE, 2020, pp. 112–114.
- [36] H. Kim, A. Handa, R. Benosman, S.-H. Ieng, and A. J. Davison, "Simultaneous mosaicing and tracking with an event camera," *J. Solid State Circ.*, vol. 43, pp. 566–576, 2008.
- [37] C. Reinbacher, G. Munda, and T. Pock, "Real-time panoramic tracking for event cameras," in *2017 IEEE International Conference on Computational Photography (ICCP)*. IEEE, 2017, pp. 1–9.
- [38] S. Guo and G. Gallego, "Cmax-slam: Event-based rotational-motion bundle adjustment and slam system using contrast maximization," *IEEE Transactions on Robotics*, 2024.
- [39] H. Kim and H. J. Kim, "Real-time rotational motion estimation with contrast maximization over globally aligned events," *IEEE Robotics and Automation Letters*, vol. 6, no. 3, pp. 6016–6023, 2021.
- [40] J. Zhang, S. Singh *et al.*, "Loam: Lidar odometry and mapping in real-time," in *Robotics: Science and systems*, vol. 2, no. 9. Berkeley, CA, 2014, pp. 1–9.
- [41] T. Shan, B. Englot, D. Meyers, W. Wang, C. Ratti, and D. Rus, "Lio-sam: Tightly-coupled lidar inertial odometry via smoothing and mapping," in *2020 IEEE/RSJ international conference on intelligent robots and systems (IROS)*. IEEE, 2020, pp. 5135–5142.
- [42] W. Xu and F. Zhang, "Fast-lio: A fast, robust lidar-inertial odometry package by tightly-coupled iterated kalman filter," *IEEE Robotics and Automation Letters*, vol. 6, no. 2, pp. 3317–3324, 2021.
- [43] C. Bai, T. Xiao, Y. Chen, H. Wang, F. Zhang, and X. Gao, "Faster-lio: Lightweight tightly coupled lidar-inertial odometry using parallel sparse incremental voxels," *IEEE Robotics and Automation Letters*, vol. 7, no. 2, pp. 4861–4868, 2022.
- [44] W. Xu, Y. Cai, D. He, J. Lin, and F. Zhang, "Fast-lio2: Fast direct lidar-inertial odometry," *IEEE Transactions on Robotics*, vol. 38, no. 4, pp. 2053–2073, 2022.
- [45] S. Guo and T. Delbruck, "Low cost and latency event camera background activity denoising," *IEEE Transactions on Pattern Analysis and Machine Intelligence*, vol. 45, no. 1, pp. 785–795, 2022.
- [46] D. Joubert, A. Marcireau, N. Ralph, A. Jolley, A. Van Schaik, and G. Cohen, "Event camera simulator improvements via characterized parameters," *Frontiers in Neuroscience*, vol. 15, p. 702765, 2021.
- [47] L. Pan, C. Scheerlinck, X. Yu, R. Hartley, M. Liu, and Y. Dai, "Bringing a blurry frame alive at high frame-rate with an event camera," in *Proceedings of the IEEE/CVF Conference on Computer Vision and Pattern Recognition*, 2019, pp. 6820–6829.
- [48] L. Pan, R. Hartley, C. Scheerlinck, M. Liu, X. Yu, and Y. Dai, "High frame rate video reconstruction based on an event camera," *IEEE Transactions on Pattern Analysis and Machine Intelligence*, vol. 44, no. 5, pp. 2519–2533, 2020.
- [49] F. Paredes-Vallés and G. C. De Croon, "Back to event basics: Self-supervised learning of image reconstruction for event cameras via photometric constancy," in *Proceedings of the IEEE/CVF Conference on Computer Vision and Pattern Recognition*, 2021, pp. 3446–3455.
- [50] G. Munda, C. Reinbacher, and T. Pock, "Real-time intensity-image reconstruction for event cameras using manifold regularisation," *International Journal of Computer Vision*, vol. 126, no. 12, pp. 1381–1393, 2018.
- [51] G. Gallego, H. Rebecq, and D. Scaramuzza, "A unifying contrast maximization framework for event cameras, with applications to motion, depth, and optical flow estimation," in *Proceedings of the IEEE conference on computer vision and pattern recognition*, 2018, pp. 3867–3876.
- [52] S. Shiba, Y. Aoki, and G. Gallego, "Event collapse in contrast maximization frameworks," *Sensors*, vol. 22, no. 14, p. 5190, 2022.
- [53] Z. Zhang, "A flexible new technique for camera calibration," *IEEE Transactions on pattern analysis and machine intelligence*, vol. 22, no. 11, pp. 1330–1334, 2000.
- [54] J. Sturm, N. Engelhard, F. Endres, W. Burgard, and D. Cremers, "A benchmark for the evaluation of rgb-d slam systems," in *2012 IEEE/RSJ international conference on intelligent robots and systems*. IEEE, 2012, pp. 573–580.
- [55] M. Grupp, "evo: Python package for the evaluation of odometry and slam." <https://github.com/MichaelGrupp/evo>, 2017.
- [56] H. Rebecq, D. Gehrig, and D. Scaramuzza, "Esim: an open event camera simulator," in *Conference on robot learning*. PMLR, 2018, pp. 969–982.
- [57] W. Xing, S. Lin, L. Yang, and J. Pan, "Target-free extrinsic calibration of event-lidar dyad using edge correspondences," *IEEE Robotics and Automation Letters*, vol. 8, no. 7, pp. 4020–4027, 2023.
- [58] D. He, W. Xu, N. Chen, F. Kong, C. Yuan, and F. Zhang, "Point-lio: Robust high-bandwidth light detection and ranging inertial odometry," *Advanced Intelligent Systems*, vol. 5, no. 7, p. 2200459, 2023.
- [59] C. Yuan, X. Liu, X. Hong, and F. Zhang, "Pixel-level extrinsic self calibration of high resolution lidar and camera in targetless environments," *IEEE Robotics and Automation Letters*, vol. 6, no. 4, pp. 7517–7524, 2021.